Biomech Model Mechanobiol (2016) 15:111–131
DOI 10.1007/s10237-015-0695-8

ORIGINAL PAPER

Stochastic multiscale modelling of cortical bone elasticity based on high-resolution imaging

Vittorio Sansalone[1] · Davide Gagliardi[1] · Christophe Desceliers[2] · Valérie Bousson[3] · Jean-Denis Laredo[3] · Françoise Peyrin[4,5] · Guillaume Haïat[1] · Salah Naili[1]

Received: 23 January 2015 / Accepted: 15 June 2015 / Published online: 23 July 2015
© Springer-Verlag Berlin Heidelberg 2015

Abstract Accurate and reliable assessment of bone quality requires predictive methods which could probe bone microstructure and provide information on bone mechanical properties. Multiscale modelling and simulation represent a fast and powerful way to predict bone mechanical properties based on experimental information on bone microstructure as obtained through X-ray-based methods. However, technical limitations of experimental devices used to inspect bone microstructure may produce blurry data, especially in in vivo conditions. Uncertainties affecting the experimental data (input) may question the reliability of the results predicted by the model (output). Since input data are uncertain, deterministic approaches are limited and new modelling paradigms are required. In this paper, a novel stochastic multiscale model is developed to estimate the elastic properties of bone while taking into account uncertainties on bone composition. Effective elastic properties of cortical bone tissue were computed using a multiscale model based on continuum micromechanics. Volume fractions of bone components (collagen, mineral, and water) were considered as random variables whose probabilistic description was built using the maximum entropy principle. The relevance of this approach was proved by analysing a human bone sample taken from the inferior femoral neck. The sample was imaged using synchrotron radiation micro-computed tomography. 3-D distributions of Haversian porosity and tissue mineral density extracted from these images supplied the experimental information needed to build the stochastic models of the volume fractions. Thus, the stochastic multiscale model provided reliable statistical information (such as mean values and confidence intervals) on bone elastic properties at the tissue scale. Moreover, the existence of a simpler "nominal model", accounting for the main features of the stochastic model, was investigated. It was shown that such a model does exist, and its relevance was discussed.

Keywords Cortical bone · Microstructure · Haversian porosity · Tissue mineral density · Elastic properties · SR-μCT imaging · Multiscale modelling · Continuum micromechanics · Stochastic modelling · MaxEnt principle · Uncertainty quantification

✉ Vittorio Sansalone
vittorio.sansalone@u-pec.fr;
vittorio.sansalone@univ-paris-est.fr

1 Laboratoire Modélisation et Simulation Multi Echelle, MSME UMR 8208 CNRS, Université Paris-Est, 61 avenue du Général de Gaulle, 94010 Créteil Cedex, France

2 Laboratoire Modélisation et Simulation Multi Echelle, MSME UMR 8208 CNRS, Université Paris-Est, 5, bd Descartes, 77454 Marne-la-Vallée, France

3 Sorbonne Paris Cité, UMR CNRS 7052 B2OA, Université Paris Diderot, 10, avenue de Verdun, 75010 Paris, France

4 CREATIS, INSERM U1044, UMR CNRS 5220, INSA Lyon, Université de Lyon, 69621 Villeurbanne Cedex, France

5 ESRF, BP 220, 38043 Grenoble Cedex, France

1 Introduction

At the organ scale, bone is organised in two compartments: the cortical and trabecular compartments, both contributing to bone strength (Manske et al. 2009). Bone strength depends on both bone quantity and bone quality (Donnelly 2011). Bone quantity refers to the amount of bone mass. Bone quality is a more subtle and hazy feature (Bouxsein 2003) encompassing multiple parameters, but, in general, it refers to the volumetric composition and microarchitecture of bone. Indeed, bone is a complex material showing a hierarchical structure spanning several length scales, from the

molecular scale to the organ one (Rho et al. 1998; Hulmes 2002; Fratzl et al. 2004). Loss of bone mass or abnormal microarchitecture—often associated with bone diseases such as osteoporosis—may lead to reduced bone strength and increased risk of fracture.

In clinical practice, the bone mineral density (BMD) at the hip—as measured with dual X-ray absorptiometry (DXA) techniques—is still considered as the gold standard for assessing the risk of fracture. However, BMD only measures bone mass (i.e. bone quantity) but is unable to assess microstructural features such as volumetric bone composition and microarchitecture (i.e. bone quality). Several studies have shown Haversian porosity (HP) and tissue mineral density (TMD) to be among the most relevant determinants of bone strength and associated fracture risk (Burr 2004; Currey 1988; Bell et al. 1999; Vajda and Bloebaum 1999; Bousson et al. 2001; Crabtree et al. 2001; Sasso et al. 2008; Zebaze et al. 2010). HP and TMD describe different features of bone microstructure. HP refers to the volume fraction of Haversian and Volkmann's canals (typical diameter of several tens to a few hundreds micrometres) in bone tissue. TMD represents the degree of mineralisation of the solid bone matrix (Boivin and Meunier 2002; Bouxsein et al. 2010).

In the femoral neck, a critical anatomical site for osteoporotic fractures, osteoporotic bone structure is characterised by progressive thinning of the cortical shell and loss of trabecular mass (Mayhew et al. 2005). Spatial variations of HP and TMD in the femoral hip region induce heterogeneity of cortical bone at the organ scale (Bensamoun et al. 2004a, b; Yamato et al. 2006; Sasso et al. 2007, 2008; Mathieu et al. 2013). This heterogeneity strongly affects the mechanical response of bone as it was widely documented by studies on ultrasonic wave propagation (Haiat et al. 2009, 2011; Naili et al. 2010; Grimal et al. 2014) and nanoindentation (Yao et al. 2011; Vayron et al. 2012, 2014).

Establishing reliable mathematical relationships between available experimental data (BMD, HP, TMD, etc.) and mechanical properties (stiffness, strength, etc.) is important to predict the fracture risk. In this respect, multiscale modelling and simulation approaches can be useful to account for the specific volumetric composition and organisation of bone components at each scale. Several multiscale approaches have been proposed to model the mechanical properties of bone tissue, including continuum micromechanics (Hellmich et al. 2004b; Fritsch and Hellmich 2007; Grimal et al. 2011b; Parnell et al. 2012), asymptotic homogenisation (Aoubiza et al. 1996; Parnell et al. 2012; Predoi-Racila and Crolet 2008), and other techniques (Yoon and Cowin 2008a, b; Ghanbaria and Naghdabadi 2009).

Recently, a multiscale model based on continuum micromechanics was proposed by our group to estimate the elastic properties of bone tissue (Sansalone et al. 2010, 2012a, b). The experimental information was obtained using synchrotron radiation micro-computed tomography (SR-μCT) which provided a 3-D mapping of the HP and TMD with a spatial resolution of about 10 μm. The SR-μCT images were used to determine the heterogeneous composition of bone and, in turn, to compute the heterogeneous elastic properties of one (Sansalone et al. 2010, 2012b) or several (Sansalone et al. 2012a) bone samples obtained from the inferior femoral neck of elderly patients.

Experimental information which can be obtained in vivo through standard medical devices such as DXA devices or quantitative CT (QCT) is much less accurate. Lack of accuracy is related to a low spatial resolution and polyenergetic X-ray beam. In any case, the lower the accuracy of the experimental data, the higher the uncertainty affecting the values of the derived modelling parameters. Uncertainty on the modelling parameters increases with zooming down into the nanostructure of bone. Current in vivo experimental techniques cannot easily provide accurate information about the morphology, volumetric content, spatial arrangement, and mechanical behaviour of bone components. For instance, orientation of the collagen as well as size, shape, and organisation of the hydroxyapatite mineral in the bone lamellae remain largely uncovered. (Collagen and mineral are the two major components of bone solid matrix.) Only recent breakthroughs in synchrotron tomographic imaging have given access to direct 3-D information on the bone structure at the nanoscale level (Langer et al. 2012; Varga et al. 2013).

Dealing with uncertain data requires new modelling paradigms. There exist several approaches to take into account such uncertainties among which the theory of probability (Arnold 1973; Feller 1971; Halmos 1976; Krée and Soize 1986) has proved, during last decades, its efficiency and robustness. In particular, the maximum entropy (MaxEnt) principle (Jumarie 2000; Kapur and Kesavan 1992) was successfully applied to several problems of elasticity to build robust probability distributions of random variables and random fields ensuring both the mathematical and the physical consistency of the probabilistic descriptions (Soize 2006, 2008, 2001; Guilleminot et al. 2011; Guilleminot and Soize 2012, 2013a, b).

Uncertainties of model parameters is an important problem in biomechanics at all scales. Modelling uncertainties and computing stochastic responses may be useful to assess robustness of subject-specific predictive models in musculoskeletal biomechanics (Valente et al. 2014). Aiming at characterising the mechanical properties of bone in vivo, *both* hierarchical structure of bone *and* the uncertainties existing on experimental data should account for. So far, there are only a few research works having addressed these two issues at once. A stochastic multiscale method based on asymptotic homogenisation theory was recently proposed to take into account the uncertainties caused by image-based modelling and trabecular stiffness orientation in predicting the

elastic moduli of trabecular bone (Basaruddin et al. 2015). Another contribution was recently proposed by our group by introducing a stochastic treatment of the elastic properties of bone components in a multiscale model of bone solid matrix based on continuum micromechanics theory (Sansalone et al. 2014). Therein, in the framework of a parametric probabilistic approach, elastic coefficients of bone components were considered as random variables and their probability density functions (PDFs) obtained using the MaxEnt principle.

In this work, we address the complementary issue of uncertainty on volumetric bone composition. Aiming at moving towards in vivo applications, uncertainty on subject-specific bone microstructure has to be taken into account to estimate the mechanical properties of bone. In this respect, two main goals will be pursued in this paper.

The *first goal* of this paper is to describe a new modelling approach suitable to estimate bone elastic properties while taking into account uncertainties on the composition of bone microstructure. Following the ideas set forth in the scope of uncertain elastic properties of bone components (Sansalone et al. 2014), we will develop a stochastic multiscale model of cortical bone by introducing a stochastic treatment of the volume fractions of bone components in the multiscale model of bone developed by our group (Sansalone et al. 2010). PDFs of the volume fractions will be constructed using the MaxEnt principle and available experimental data. Our experimental data are represented by statistical information on the 3-D distributions of HP and TMD obtained by analysis of high-resolution SR-μCT images of one bone sample of the inferior femoral neck of an elderly patient. It will be shown that this approach can effectively describe the elastic properties of cortical bone at the organ scale. The final outcome of the model is given in terms of expected values, confidence intervals, and other statistics of these properties.

Granted the suitability of the stochastic model, the *second goal* is to understand whether a simpler description is possible. To this aim, we will assess to which extent the stochastic model could be described by a simpler, deterministic model. Indeed, the computational cost of the stochastic model is quite high, and there is an interest for computationally spare alternatives. We will focus on two questions: Does a simpler model exist, providing "good" estimates of expected elastic properties of bone? If so, how accurate and reliable are these estimates? We will show that such a model exists and discuss its relevance.

The paper is organised as follows. The stochastic multiscale model of bone is presented in Sect. 2. This section is introduced by a brief presentation of the experimental data used to develop the model. Then, the theoretical development and the solution algorithm of the stochastic multiscale model are presented in detail. A simpler nominal model and a finite element model are also presented. Numerical results are thoroughly presented in Sect. 3 bringing up the relevance of the different modelling approaches proposed. In Sect. 4, the findings of this study are discussed focusing on the two goals set forth. Limitations and further developments are also addressed. Eventually, in Sect. 5 the conclusions of this work are drawn, focusing on the two goals set forth, and its limitations and further developments are discussed.

2 Materials and methods

2.1 Experimental data

2.1.1 Preparation and imaging of the bone sample

The experimental procedure for preparing and imaging the bone sample was thoroughly presented elsewhere (Sansalone et al. 2010). We recall here below the key points for sake of completeness and refer to that paper for more details.

A bone sample was extracted from the inferior femoral neck of a 79-year-old patient during standard hemiarthroplasty. The bone sample was imaged using synchrotron radiation micro-computed tomography (SR-μCT) at the European Synchrotron Radiation Facility (ESRF, Grenoble, France). The sample was imaged at the ID19 beamline using a monochromatic X-ray beam tuned at 25 KeV. The 3-D image was reconstructed using a customised filtered back-projection algorithm developed at ESRF. The outcome was a 3-D grayscale (range [0, 255]) mapping of the linear attenuation μ of the monochromatic X-ray beam at 25 KeV. The reconstruction was performed in a volume of interest of $660 \times 660 \times 523$ isotropic voxels (size 10.13 μm). The 3-D volume reconstructed is shown in Fig. 1. A Cartesian frame is also shown. The unit vector $\mathbf{e}_3$ is aligned with the axis of the femoral neck, and the unit vectors $\mathbf{e}_1$ and $\mathbf{e}_2$ lie in the plane of the cross section of the sample.

The grayscale 3-D mapping was analysed in order to separate two regions: the voids (HP and space surrounding the sample) and the solid matrix of bone. Voxels having a grayscale level higher than a fixed threshold were assigned

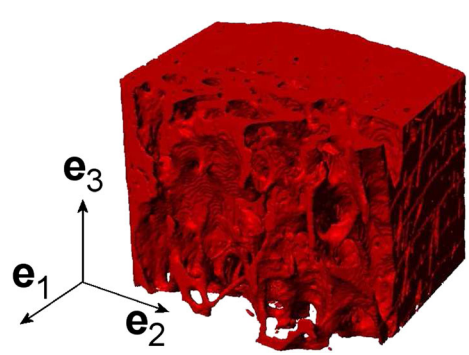

Fig. 1 Reconstructed 3-D model of the bone sample and Cartesian frame

to the bone matrix region, whereas the others were assigned to the void region. In this study, the threshold was fixed to 130. (The value of the threshold was found not to significantly affect the elastic coefficients of bone tissue as predicted by the model described below in Sect. 2.2.1.) Grayscale levels in the bone matrix region were converted in a 3-D voxel-wise mapping of tissue mineral density (TMD) thanks to the linear relationship existing between the X-ray beam attenuation μ and the TMD, reading $\mu = 3.32\,\text{TMD} + 0.51$, where μ is expressed in cm^{-1} and the TMD is expressed in g/cm^3. This expression was calibrated using the theoretical values for hydroxyapatite and water at 25 KeV of the DABAX database. A detailed description of the segmentation process can be found in the appendix of Sansalone et al. (2010).

2.1.2 Data analysis: HP and TMD

In previous work (Sansalone et al. 2010, 2012b), HP and TMD were analysed in radial regions of interest (RoIs) and axial slices (radial and axial directions refer to the anatomical axis of the sample). The thickness of RoIs and slices was 50 voxels (i.e. about half a millimetre). In this work, a finer analysis is performed. HP and TMD have been analysed in several cubic representative volume elements (RVEs) with edges of about half a millimetre (equal to the thickness of the RoIs and slices of our previous studies).

SimpleWare 5.0 ScanIP+ ™ software was used to extract and analyse $N_{\text{RVE}} = 12$ cubic RVEs from the 3-D model of the bone sample. Positions of the RVEs were chosen in order to span the whole cortical region of the sample, see Fig. 2. RVEs were extracted at about 1.5 mm from the periosteum (distance measured with respect to the centre of the RVEs) and at different hoop and axial positions with respect to a cylindrical frame centred at the anatomical axis of the bone sample. Let θ be the angular coordinate in the cross section plane $(\mathbf{e}_1, \mathbf{e}_2)$ and z be an abscissa along the femoral neck axis $\mathbf{e}_3$. Coordinates of the centre of the RVEs were set at $\theta \in \{-40, -20, 0, 20\}^\circ$ (with 0° being the inferior axis of the femoral neck) and $z \in \{1.5, 3.5, 5.5\}$ mm (distance from the distal part of the sample). RVEs were oriented following a circular arc corresponding to the anatomical hoop direction of the sample.

Each RVE was analysed to compute its HP and TMD. The HP is meaningful at the scale of the tissue, whereas the TMD is defined at the voxel scale (within the solid bone matrix only) and is heterogeneous within each RVE. Therefore, one scalar value of HP and a 3-D voxel-wise distribution of TMD were obtained for each RVE. All the RVEs were also analysed collectively to obtain experimental information representative of the whole cortical region. Recalling that one RVE represents one material point at the organ scale, hereinafter terms *local* and *global* will refer to one RVE and all the RVEs, respectively.

Then, several experimental databases were constituted: (*i*) one global database collecting the N_{RVE} values of HP; (*ii*) one local database for each RVE collecting the voxel-wise values of TMD within the solid matrix; let N^i_{vox} be the number of TMD values for the ith RVE; (*iii*) one global database of TMD gathering the TMD databases of all the RVEs, for a total of $N_{\text{vox}} = \sum_{i=1}^{N_{\text{RVE}}} N^i_{\text{vox}}$ voxel-wise values of TMD. Note that the N_{RVE} databases (*ii*) refer to one RVE, whereas the two databases (*i*) and (*iii*) refer to the whole cortical region.

These experimental databases were further used to compute the volume fractions of bone components as explained in Sect. 2.2.5. Moreover, statistics on the experimental databases of HP and TMD were computed. In particular, the mean values and dispersions of experimental data will be referred to as $\mu_{\text{exp}}(\bullet)$ and $\delta_{\text{exp}}(\bullet)$, respectively, where $\bullet$ is either HP or TMD.

2.2 Model

A stochastic multiscale model of cortical bone was developed by introducing a stochastic treatment of some modelling parameters (volume fractions of bone components) in the deterministic multiscale model proposed in previous work by our group (Sansalone et al. 2010, 2012a, b).

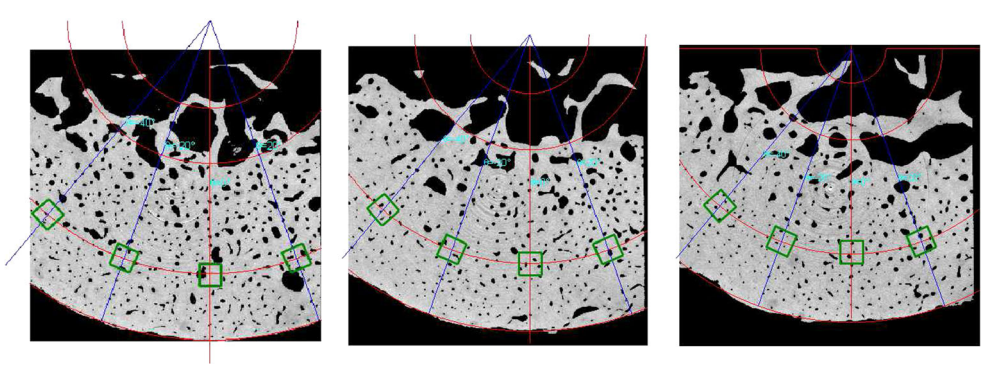

Fig. 2 From *left to right* Three cross sections of the bone sample at $z = 150, 350, 550\ \mu\text{m}$, respectively. RVEs are marked by *green squares*

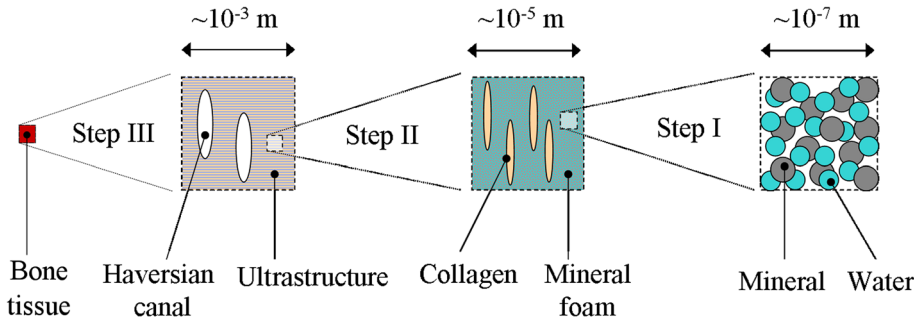

Fig. 3 Sketch of the multiscale model

2.2.1 *Deterministic multiscale model of cortical bone*

A multiscale model was recently proposed by our group to study bone elasticity at the organ scale (Sansalone et al. 2010). Extending the ideas set forth by Hellmich and coworkers (Hellmich et al. 2004a), the model uses a continuum micromechanics approach (Suquet 1997; Nemat-Nasser and Hori 1999) to estimate elastic properties of cortical bone at the tissue scale. In the framework of continuum micromechanics, the homogenised elastic tensor $\mathbb{C}_{\text{hom}}$ of a multiphase medium can be computed by solving the equation (Sansalone et al. 2014):

$$g(\mathbb{C}_{\text{hom}}; \{f_r\}, \{\mathbb{C}_r\}) = 0\,, \quad r = 1, \ldots, N_{\text{ph}} \tag{1}$$

where $\{f_r\}$ and $\{\mathbb{C}_r\}$ are the volume fractions and elastic tensors of the N_{ph} constituent phases, respectively.

The multiscale model considers three scales below the organ scale: the cortical tissue (characteristic length of several hundred micrometres), made of cylindrical pores embedded in the bone ultrastructure—the solid bone matrix; the ultrastructure (several micrometres), made of cylindrical collagen molecules embedded in a mineral foam; and the mineral foam (few hundred nanometres), made of hydroxyapatite (HA) crystals interpenetrated by water-filled spaces. All the components were considered as elastically isotropic, and their properties were taken from Kotha and Guzelsu (2000). The multiscale model is depicted in Fig. 3 where the four scales and the three homogenisation steps (see below) are sketched.

The following cascade of formal problems—corresponding to three homogenisation steps—has to be solved in order to compute the elastic tensor of cortical tissue $\mathbb{C}_{\text{cort}}$:

$$g_{\text{I}}^{\text{SC}}\left(\mathbb{C}_{\text{foam}}; \left\{f_{\text{HA}}^{\text{foam}}, f_{\text{w}}^{\text{foam}}\right\}, \{\mathbb{C}_{\text{HA}}, \mathbb{C}_{\text{w}}\}\right) = 0 \rightarrow \mathbb{C}_{\text{foam}}\,, \tag{2}$$

$$g_{\text{II}}^{\text{MT}}\left(\mathbb{C}_{\text{ultra}}; \left\{f_{\text{col}}^{\text{ultra}}, f_{\text{foam}}^{\text{ultra}}\right\}, \{\mathbb{C}_{\text{col}}, \mathbb{C}_{\text{foam}}\}\right) = 0 \rightarrow \mathbb{C}_{\text{ultra}}\,, \tag{3}$$

$$g_{\text{III}}^{\text{MT}}\left(\mathbb{C}_{\text{cort}}; \left\{f_{\text{pore}}^{\text{cort}}, f_{\text{ultra}}^{\text{cort}}\right\}, \{\mathbb{C}_{\text{pore}}, \mathbb{C}_{\text{ultra}}\}\right) = 0 \rightarrow \mathbb{C}_{\text{cort}}. \tag{4}$$

Superscripts SC and MT refer to the self-consistent and Mori–Tanaka schemes, respectively, which are used at the different scales to compute the homogenised elastic tensors. The self-consistent scheme is implicit. Therefore, Eq. (2) has to be solved iteratively for $\mathbb{C}_{\text{foam}}$. The Mori–Tanaka scheme is explicit. Therefore, Eq. (3) and Eq. (4) can be explicitly solved for $\mathbb{C}_{\text{ultra}}$ and $\mathbb{C}_{\text{cort}}$, respectively.

In Eq. (2), $f_{\text{HA}}^{\text{foam}}$ and $f_{\text{w}}^{\text{foam}} = 1 - f_{\text{HA}}^{\text{foam}}$ are the volume fractions of HA mineral and water in the mineral foam, respectively. In Eq. (3), $f_{\text{col}}^{\text{ultra}}$ and $f_{\text{foam}}^{\text{ultra}} = 1 - f_{\text{col}}^{\text{ultra}}$ are the volume fractions of collagen and mineral foam in the ultrastructure, respectively. In Eq. (4), $f_{\text{pore}}^{\text{cort}}$ and $f_{\text{ultra}}^{\text{cort}} = 1 - f_{\text{pore}}^{\text{cort}}$ are the volume fractions of the Haversian pores and ultrastructure in the cortical tissue, respectively. A similar notation is used for the elastic tensors. Thus, $\mathbb{C}_{\text{HA}}$, $\mathbb{C}_{\text{w}}$, $\mathbb{C}_{\text{col}}$, and $\mathbb{C}_{\text{pore}}$ are the elastic tensors of the HA mineral, water, collagen, and Haversian pores, respectively. Moreover $\mathbb{C}_{\text{foam}}$, $\mathbb{C}_{\text{ultra}}$, and $\mathbb{C}_{\text{cort}}$ are the homogenised elastic tensors of the mineral foam, ultrastructure, and cortical tissue, respectively.

2.2.2 *Probabilistic model of the uncertain volume fractions*

Using deterministic models assumes that the modelling parameters are well identified. However, most of the time, only partial information is available on these parameters and their actual values, obtained through experimental measurements, are uncertain. Among others approaches, probability theory provides an effective and robust framework to take into account such uncertainties (Feller 1971; Arnold 1973; Halmos 1976; Krée and Soize 1986).

In the framework of a parametric probabilistic approach, uncertainties on a modelling parameter x are taken into account by replacing x by a real-valued random variable X. (Hereafter, capital letters will refer to random variables.) It is assumed that the probability law of X is defined by a probability density function (PDF) $x \mapsto p_X(x)$ on $\mathbb{R}$ (the set of the real numbers). The construction of the probability law of the random variables must be carefully carried out in order to embed the available statistical information on x and to respect well posedness of the elasticity problem. In this paper, the

construction of the probabilistic model is carried out by using the MaxEnt principle (Jaynes 1957a, b; Jumarie 2000; Kapur and Kesavan 1992; Soize 2001). In the context of the information theory, entropy has been introduced as a measure of the uncertainty for probability distributions (Shannon 1948), and the MaxEnt principle consists in maximising this entropy subjected to constraints defined by the available information. The entropy associated with the PDF p_X is defined as:

$$S(p_X) = -\int_{\mathbb{R}} p_X(x) \log\left(p_X(x)\right) \, \mathrm{d}x \tag{5}$$

The MaxEnt principle was used to model uncertainties on the elastic moduli of bone components in previous work (Sansalone et al. 2014). Hereinafter, the same strategy is used to account for uncertainties on the volume fractions only. Let x be either of the volume fractions $f_{\mathrm{HA}}^{\mathrm{foam}}$, $f_{\mathrm{col}}^{\mathrm{ultra}}$, and $f_{\mathrm{pore}}^{\mathrm{cort}}$. Thus, the uncertain variable x is modelled by a random variable X with PDF p_X. The available information on X is assumed to be: (*i*) the support of X is $\mathcal{S}_X = [0, 1]$; (*ii*) the mean value of X is μ_X; (*iii*) the dispersion of X is $\delta_X = \sigma_X/\mu_X$, where σ_X is the standard deviation of X. The normalisation condition of the PDF and above constraints read:

$$\int_{[0,1]} p_X(x) \, \mathrm{d}x = 1 \, , \tag{6}$$

$$\int_{[0,1]} x \, p_X(x) \, \mathrm{d}x = \mu_X \, , \tag{7}$$

$$\int_{[0,1]} x^2 \, p_X(x) \, \mathrm{d}x = (1 + \delta_X^2) \cdot \mu_X^2 \, . \tag{8}$$

In our case, the MaxEnt principle consists in maximising the entropy in Eq. (5) subjected to constraints in Eqs. (6)–(8). The ensuing form of the PDF turns out to be:

$$p_X^{\boldsymbol{\lambda}^\star}(x) = \mathbb{1}_{[0,1]}(x) \, e^{-\lambda_0^\star - \lambda_1^\star x - \lambda_2^\star x^2} \, , \tag{9}$$

where the vector $\boldsymbol{\lambda}^\star = \{\lambda_0^\star, \lambda_1^\star, \lambda_2^\star\}$ collects the Lagrange multipliers associated with the constraints in Eqs. (6)–(8), respectively. It can be shown that $\boldsymbol{\lambda}^\star$ can be obtained by minimising the Hamiltonian function defined by:

$$\begin{aligned} \mathcal{H}(\boldsymbol{\lambda}) \; := \; & \lambda_0 + \lambda_1 \, \mu_X + \lambda_2 \, (1 + \delta_X^2) \, \mu_X^2 \\ & + \textstyle\int_{[0,1]} e^{-\lambda_0 - \lambda_1 x - \lambda_2 x^2} \, \mathrm{d}x \, . \end{aligned} \tag{10}$$

Therefore, the solution vector $\boldsymbol{\lambda}^\star$ reads:

$$\boldsymbol{\lambda}^\star = \arg\min_{\boldsymbol{\lambda} \in \mathbb{R}^3} \mathcal{H}(\boldsymbol{\lambda}) \, , \tag{11}$$

where the operator arg min stands for the argument of the minimum.

2.2.3 Stochastic multiscale model of cortical bone

The stochastic multiscale model of cortical bone is constructed by substituting the volume fractions $f_{\mathrm{HA}}^{\mathrm{foam}}$, $f_{\mathrm{col}}^{\mathrm{ultra}}$, and $f_{\mathrm{pore}}^{\mathrm{cort}}$ by the random variables $F_{\mathrm{HA}}^{\mathrm{foam}}$, $F_{\mathrm{col}}^{\mathrm{ultra}}$, and $F_{\mathrm{pore}}^{\mathrm{cort}}$ in Eq. (2) (homogenisation step I), Eq. (3) (homogenisation step II), and Eq. (4) (homogenisation step III), respectively. Thus, the stochastic versions of these equations read:

$$g_{\mathrm{I}}(\mathbb{C}_{\mathrm{foam}}; F_{\mathrm{HA}}^{\mathrm{foam}}, \{\mathbb{c}_{\mathrm{HA}}, \mathbb{c}_{\mathrm{w}}\}) = 0 \rightarrow \mathbb{C}_{\mathrm{foam}} \, , \tag{12}$$

$$g_{\mathrm{II}}(\mathbb{C}_{\mathrm{ultra}}; F_{\mathrm{col}}^{\mathrm{ultra}}, \{\mathbb{c}_{\mathrm{col}}, \mathbb{C}_{\mathrm{foam}}\}) = 0 \rightarrow \mathbb{C}_{\mathrm{ultra}} \, , \tag{13}$$

$$g_{\mathrm{III}}(\mathbb{C}_{\mathrm{cort}}; F_{\mathrm{pore}}^{\mathrm{cort}}, \{\mathbb{c}_{\mathrm{pore}}, \mathbb{C}_{\mathrm{ultra}}\}) = 0 \rightarrow \mathbb{C}_{\mathrm{cort}} \, . \tag{14}$$

For sake of simplicity, only the independent random volume fractions were introduced in the above equations. Since the volume fractions are random variables, the homogenised elastic tensors of the mineral foam ($\mathbb{C}_{\mathrm{foam}}$), ultrastructure ($\mathbb{C}_{\mathrm{ultra}}$), and cortical tissue ($\mathbb{C}_{\mathrm{cort}}$) turn out to be random tensors.

2.2.4 Nominal multiscale model of cortical bone

The stochastic multiscale model can be compared with a *nominal model* obtained using *nominal* values of the volume fractions. The nominal model would refer to the whole cortical region. Therefore, nominal values of the volume fractions were set to their global experimental mean values. Using these input data in the deterministic model of Eqs. (2)–(4), the *nominal elastic tensors* are obtained:

$$g_{\mathrm{I}}(\mathbb{c}_{\mathrm{foam}}^{\mu}; \mu_{\mathrm{exp}}(f_{\mathrm{HA}}^{\mathrm{foam}}), \{\mathbb{c}_{\mathrm{HA}}, \mathbb{c}_{\mathrm{w}}\}) = 0 \rightarrow \mathbb{c}_{\mathrm{foam}}^{\mu} \, , \tag{15}$$

$$g_{\mathrm{II}}(\mathbb{c}_{\mathrm{ultra}}^{\mu}; \mu_{\mathrm{exp}}(f_{\mathrm{col}}^{\mathrm{ultra}}), \{\mathbb{c}_{\mathrm{col}}, \mathbb{c}_{\mathrm{foam}}^{\mu}\}) = 0 \rightarrow \mathbb{c}_{\mathrm{ultra}}^{\mu} \, , \tag{16}$$

$$g_{\mathrm{III}}(\mathbb{c}_{\mathrm{cort}}^{\mu}; \mu_{\mathrm{exp}}(f_{\mathrm{pore}}^{\mathrm{cort}}), \{\mathbb{c}_{\mathrm{pore}}, \mathbb{c}_{\mathrm{ultra}}^{\mu}\}) = 0 \rightarrow \mathbb{c}_{\mathrm{cort}}^{\mu} \, , \tag{17}$$

where $\mathbb{c}_{\mathrm{foam}}^{\mu}$, $\mathbb{c}_{\mathrm{ultra}}^{\mu}$, and $\mathbb{c}_{\mathrm{cort}}^{\mu}$ are the nominal elastic tensors of the mineral foam, ultrastructure, and cortical tissue, respectively.

2.2.5 Model parameters

The multiscale model previously described allows estimating the effective elastic tensor of an RVE of cortical bone (tissue scale) based on the local values of some modelling parameters describing the local bone microstructure. In this work, cubic RVEs are considered, see Sect. 2.1.2. Modelling parameters are the elastic tensors and volume fractions of bone elementary components. Additional assumptions are made on the geometric arrangement of bone components at the different scales (Sansalone et al. 2010), leading to different

expressions of the Eshelby tensors (Eshelby 1957; Suvorov and Dvorak 2002) underlying functions g_{I}, g_{II}, and g_{III}.

For sake of simplicity, all the bone components were considered as linearly elastic, isotropic materials. Elastic tensors of HA mineral ($\mathbb{c}_{\mathrm{HA}}$), water ($\mathbb{c}_{\mathrm{w}}$), and collagen ($\mathbb{c}_{\mathrm{col}}$) were constructed using data taken from Kotha and Guzelsu (2000). Moreover, Haversian pores were considered as saturated by water; thus $\mathbb{c}_{\mathrm{pore}} = \mathbb{c}_{\mathrm{w}}$.

Volume fractions $f_{\mathrm{HA}}^{\mathrm{foam}}$, $f_{\mathrm{col}}^{\mathrm{ultra}}$, and $f_{\mathrm{pore}}^{\mathrm{cort}}$ were computed based on experimental measures of HP and TMD (Sansalone et al. 2010). Values of HP and TMD were analysed: (*i*) in each RVE—in order to obtain *local* statistical information representative of one RVE; (*ii*) gathering the data of all the RVEs—in order to obtain *global* statistical information representative of the whole cortical region.

Individual RVEs were analysed first. Within each RVE, the volume fraction of Haversian pores, $f_{\mathrm{pore}}^{\mathrm{cort}}$, is equal to the HP. Thus, one value of $f_{\mathrm{pore}}^{\mathrm{cort}}$ is obtained for each RVE. Moreover, $f_{\mathrm{col}}^{\mathrm{ultra}}$ and $f_{\mathrm{HA}}^{\mathrm{foam}}$ were computed from the voxel-wise 3-D distribution of TMD, leading to a voxel-wise 3-D distribution of these volume fractions in the bone solid matrix. First, volume fractions of collagen, HA, and water were computed at the scale of the ultrastructure:

$$\begin{cases} f_{\mathrm{HA}}^{\mathrm{ultra}} = \mathrm{TMD}/\rho_{HA}\,, \\ f_{\mathrm{col}}^{\mathrm{ultra}} + f_{\mathrm{HA}}^{\mathrm{ultra}} + f_{\mathrm{w}}^{\mathrm{ultra}} = 1\,, \\ \dfrac{f_{\mathrm{col}}^{\mathrm{ultra}}}{f_{\mathrm{w}}^{\mathrm{ultra}}} = 0.36 + 0.084\,\mathrm{e}^{6.7 f_{\mathrm{HA}}^{\mathrm{ultra}}}\,, \end{cases} \tag{18}$$

where ρ_{HA} is the mass density of the HA and the third equation is an empirical relation obtained through measurements of volume fractions in demineralised bone (Broz et al. 1995). Then, volume fractions of HA and water were computed at the scale of the mineral foam as:

$$\begin{cases} f_{\mathrm{HA}}^{\mathrm{foam}} = \dfrac{f_{\mathrm{HA}}^{\mathrm{ultra}}}{f_{\mathrm{HA}}^{\mathrm{ultra}} + f_{\mathrm{w}}^{\mathrm{ultra}}}\,, \\ f_{\mathrm{w}}^{\mathrm{foam}} = \dfrac{f_{\mathrm{w}}^{\mathrm{ultra}}}{f_{\mathrm{HA}}^{\mathrm{ultra}} + f_{\mathrm{w}}^{\mathrm{ultra}}}\,. \end{cases} \tag{19}$$

For the ith RVE, the outcome is one value of $f_{\mathrm{pore}}^{\mathrm{cort}}$ and two databases collecting the N_{vox}^{i} values of $f_{\mathrm{col}}^{\mathrm{ultra}}$ and $f_{\mathrm{HA}}^{\mathrm{foam}}$ at each voxel of the solid matrix. Statistics on these databases were computed, namely the mean values $\mu_{\mathrm{exp}}(\bullet)$ and dispersions $\delta_{\mathrm{exp}}(\bullet)$, with $\bullet \in \{f_{\mathrm{col}}^{\mathrm{ultra}}, f_{\mathrm{HA}}^{\mathrm{foam}}\}$.

The data of all the RVEs were further gathered to obtain three global databases of the volume fractions. The global database of $f_{\mathrm{pore}}^{\mathrm{cort}}$ was made of the N_{RVE} items, whereas the global databases of $f_{\mathrm{col}}^{\mathrm{ultra}}$ and $f_{\mathrm{HA}}^{\mathrm{foam}}$ were made of N_{vox} items. Statistics on these databases were computed, namely the mean values $\mu_{\mathrm{exp}}(\bullet)$ and dispersions $\delta_{\mathrm{exp}}(\bullet)$, with $\bullet \in \{f_{\mathrm{pore}}^{\mathrm{cort}}, f_{\mathrm{col}}^{\mathrm{ultra}}, f_{\mathrm{HA}}^{\mathrm{foam}}\}$. These global experimental statistics were used as *available information* to build the stochastic model of the random volume fractions described in Sect. 2.2.2, see Step I of the solution algorithm described in Sect. 2.2.6.

It should be noted that the multiscale model described above requires individual phases to be homogeneous within the RVE at each scale. This implies that only one value of $f_{\mathrm{HA}}^{\mathrm{foam}}$, $f_{\mathrm{col}}^{\mathrm{ultra}}$, and $f_{\mathrm{pore}}^{\mathrm{cort}}$ can be considered for the whole solid matrix of the RVE. Since $f_{\mathrm{HA}}^{\mathrm{foam}}$ and $f_{\mathrm{col}}^{\mathrm{ultra}}$ are heterogeneous within the RVE, an effective value has to be selected to make computations. In the deterministic case, it is customary to take the local mean values as representative of the underlying heterogeneous distributions. This was the choice made in our nominal model of Sect. 2.2.4.

2.2.6 Numerical solution of the stochastic multiscale model

The system of stochastic equations Eqs. (12)–(14) was solved in three steps.

Step 1/PDFs of the random volume fractions. First, the PDFs of the random volume fractions $F_{\mathrm{pore}}^{\mathrm{cort}}$, $F_{\mathrm{col}}^{\mathrm{ultra}}$, and $F_{\mathrm{HA}}^{\mathrm{foam}}$ were determined. This requires computing the parameters $\lambda_0^\star$, $\lambda_1^\star$, and $\lambda_2^\star$ appearing in Eq. (9). This step was performed using the built-in optimisation functions of MATLAB (version R2007b) software to solve the constrained optimisation problem in Eq. (11) and obtain the solution vector $\boldsymbol{\lambda}^\star = \{\lambda_0^\star, \lambda_1^\star, \lambda_2^\star\}$. Constraints associated with Eqs. (7)–(8) require the mean values and dispersions of the random volume fractions. The mean value and dispersion of the random volume fraction X (any of $F_{\mathrm{pore}}^{\mathrm{cort}}$, $F_{\mathrm{col}}^{\mathrm{ultra}}$, and $F_{\mathrm{HA}}^{\mathrm{foam}}$) were estimated by the *global* statistics of the experimental values of x (any of $f_{\mathrm{pore}}^{\mathrm{cort}}$, $f_{\mathrm{col}}^{\mathrm{ultra}}$, and $f_{\mathrm{HA}}^{\mathrm{foam}}$), that is we set:

$$\mu_X := \mu_{\mathrm{exp}}(x)\,, \quad \delta_X := \delta_{\mathrm{exp}}(x)\,. \tag{20}$$

Step 2/statistically independent realisations of the random volume fractions. Second, a large number N of statistically independent realisations of the random volume fractions were computed using the Monte Carlo method (Knuth 1981; Rubinstein 1981). In particular, the pseudo-inverse method (Devroye 1986) was used to sample the support of the random volume fractions (the unit interval) according to the PDF given in Eq. (9) and with the values of $\boldsymbol{\lambda}$ computed in the previous step. In brief, statistically independent realisations $X(a_i)$ $(i = 1, \ldots, N)$ of random variable X are obtained as:

$$X(a_i) = \left(F_X^{\boldsymbol{\lambda}}\right)^{-1}(U(a_i))\,, \tag{21}$$

where $F_X^{\boldsymbol{\lambda}}(x) = \int_0^x p_X^{\boldsymbol{\lambda}}(\xi)\,\mathrm{d}\xi$ is the cumulative density function of X and $U(a_i)$ is a realisation of a uniform random

variable U with values in $[0, 1]$. The outcome was three databases of N statistically independent realisations of the random volume fractions, that is: $\{F_{\mathrm{HA}}^{\mathrm{foam}}(a_i)\}$, $\{F_{\mathrm{col}}^{\mathrm{ultra}}(a_i)\}$, and $\{F_{\mathrm{pore}}^{\mathrm{cort}}(a_i)\}$.

Statistical estimators of the statistics of the random volume fractions $F_{\mathrm{HA}}^{\mathrm{foam}}$, $F_{\mathrm{col}}^{\mathrm{ultra}}$, and $F_{\mathrm{pore}}^{\mathrm{cort}}$ were computed using these databases. In particular, the statistical estimators of the mean value, standard deviation, and dispersion of the random volume fraction X are defined as:

$$\mu_N(X) = \frac{1}{N} \sum_{i=1}^{N} X(a_i)\,, \tag{22}$$

$$\sigma_N(X) = \left\{ \frac{1}{N-1} \sum_{i=1}^{N} (X(a_i) - \mu_N(X))^2 \right\}^{\frac{1}{2}}\,, \tag{23}$$

$$\delta_N(X) = \frac{\sigma_N(X)}{\mu_N(X)}\,. \tag{24}$$

Convergence of the statistical estimators of the mean values and dispersions ($\mu_N(X)$ and $\delta_N(X)$) towards the mean values and dispersions (μ_X and δ_X) of the random volume fractions was assessed. This allowed estimating the number N' of realisations needed for achieving convergence of the statistical estimators in terms of volume fractions.

Step 3/homogenisation: stochastic model. Third, N' statistically independent realisations of the random elastic tensors were computed. For each statistically independent realisation a_i ($i = 1, \ldots, N'$) of the random volume fractions, statistically independent realisations of the homogenised elastic tensors of the mineral foam, ultrastructure, and cortical tissue were obtained by solving the following formal equations successively:

$$g_{\mathrm{I}}(\mathbb{C}_{\mathrm{foam}}(a_i);\, F_{\mathrm{HA}}^{\mathrm{foam}}(a_i), \{\mathbb{c}_{\mathrm{HA}}, \mathbb{c}_{\mathrm{w}}\}) = 0 \rightarrow \mathbb{C}_{\mathrm{foam}}(a_i)\,, \tag{25}$$

$$g_{\mathrm{II}}(\mathbb{C}_{\mathrm{ultra}}(a_i);\, F_{\mathrm{col}}^{\mathrm{ultra}}(a_i), \{\mathbb{c}_{\mathrm{col}}, \mathbb{C}_{\mathrm{foam}}(a_i)\}) = 0 \rightarrow \mathbb{C}_{\mathrm{ultra}}(a_i)\,, \tag{26}$$

$$g_{\mathrm{III}}(\mathbb{C}_{\mathrm{cort}}(a_i);\, F_{\mathrm{pore}}^{\mathrm{cort}}(a_i), \{\mathbb{c}_{\mathrm{pore}}, \mathbb{C}_{\mathrm{ultra}}(a_i)\}) = 0 \rightarrow \mathbb{C}_{\mathrm{cort}}(a_i)\,. \tag{27}$$

The outcome was three databases of N' statistically independent realisations of the homogenised elastic tensors, that is $\{\mathbb{C}_{\mathrm{foam}}(a_i)\}$, $\{\mathbb{C}_{\mathrm{ultra}}(a_i)\}$, and $\{\mathbb{C}_{\mathrm{cort}}(a_i)\}$.

Statistical estimators of the statistics (mean values, dispersions, confidence intervals, etc.) of the random elastic tensors $\mathbb{C}_{\mathrm{foam}}$, $\mathbb{C}_{\mathrm{ultra}}$, and $\mathbb{C}_{\mathrm{cort}}$ were computed using these databases as in Eqs. (22)–(24). It is worth noting that the mean value and dispersion of the random elastic tensors are not known. However, as long as convergence is reached in terms of volume fractions after N' independent realisations, it was assumed that the same would hold for the elastic tensors. Thus, statistics of the random elastic tensors were set to the statistical estimators computed after N' independent realisations, namely:

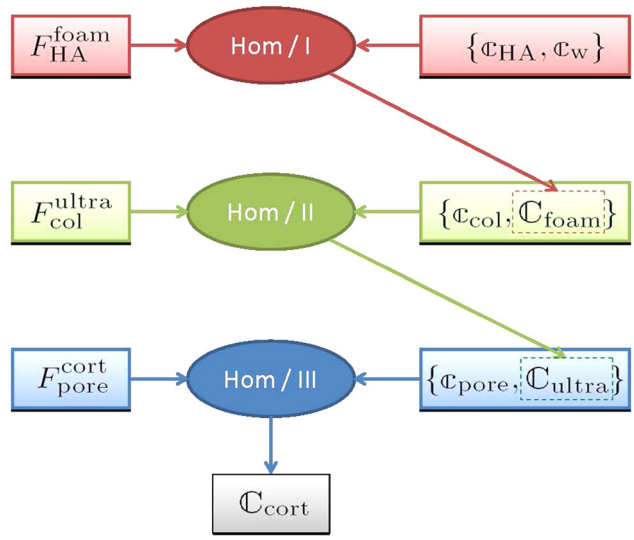

Fig. 4 Algorithm used for solving the stochastic multiscale model

$$\mu_Y := \mu_{N'}(Y)\,, \quad \delta_Y := \delta_{N'}(Y)\,, \tag{28}$$

with $Y \in \{\mathbb{C}_{\mathrm{foam}}, \mathbb{C}_{\mathrm{ultra}}, \mathbb{C}_{\mathrm{cort}}\}$.

The algorithm for computing $\mathbb{C}_{\mathrm{cort}}(a_i)$ is schematically depicted in Fig. 4 and was implemented in a MATLAB [MATLAB] code. It is worth noting that each elastic tensor $\mathbb{C}_{\mathrm{cort}}(a_i)$ is the effective elastic tensor of a *fictitious* RVE characterised by homogeneous volume fractions $F_{\mathrm{HA}}^{\mathrm{foam}}(a_i)$, $F_{\mathrm{col}}^{\mathrm{ultra}}(a_i)$, and $F_{\mathrm{pore}}^{\mathrm{cort}}(a_i)$.

Step 4/Homogenisation: nominal model. Eventually, the nominal model of Eqs. (15)–(17) was used to compute the homogenised *nominal* elastic tensors of the mineral foam, ultrastructure, and cortical tissue, that is $\mathbb{c}_{\mathrm{foam}}^{\mu}$, $\mathbb{c}_{\mathrm{ultra}}^{\mu}$, and $\mathbb{c}_{\mathrm{cort}}^{\mu}$, respectively. Nominal elastic tensors were compared with the *mean values* of the *random* elastic tensors, that is $\mu_{\mathbb{C}_{\mathrm{foam}}}$, $\mu_{\mathbb{C}_{\mathrm{ultra}}}$, and $\mu_{\mathbb{C}_{\mathrm{cort}}}$, respectively.

Comparison was made with respect to individual elastic moduli. Let y^{μ} be a nominal elastic modulus of $\mathbb{c}_{\mathrm{cort}}^{\mu}$, Y the corresponding random elastic modulus of $\mathbb{C}_{\mathrm{cort}}$, and μ_Y the mean value of Y. Elastic moduli y^{μ} and μ_Y were compared by computing their relative difference:

$$\mathrm{err}(y^{\mu}) = \left| \frac{y^{\mu} - \mu_Y}{\mu_Y} \right|\,. \tag{29}$$

2.2.7 Finite element model

Each RVE was modelled using the finite element (FE) method. A tetrahedral mesh of the 3-D geometric model

was generated using SimpleWare 5.0 FE+ ™ software. The meshing process adapted the mesh size to the geometry of the Haversian pore and solid matrix (ultrastructure) regions and accounted for the heterogeneous distribution of TMD in the solid matrix. The mesh was then exported to a text file adapted for COMSOL Multiphysics ® (version 4.2a) software. A COMSOL Multiphysics ® script was developed to compute the effective elastic tensor of the RVE. To this aim, six boundary problems of linear elasticity were solved corresponding to homogeneous axial and shear strains on the boundary of the RVE. The FE model was made of about 3×10^5 Lagrangian FEs with quadratic interpolation. For each RVE, the script performed the following steps:

1. Reading the mesh file exported by SimpleWare FE+ ™.
2. Converting the grayscale level of each mesh element into volume fractions of collagen, HA mineral, and water at the ultrastructural level, see Eq. (18).
3. Computing the elastic tensor of each mesh element of the solid matrix ($\mathbb{C}_{\text{ultra}}$) based on the volume fractions computed above and by performing the first two homogenisation steps described in Sect. 2.2.1, see Eqs. (2)–(3).
4. Setting the elastic tensor of the mesh elements belonging to the Haversian pore region to $\mathbb{C}_{\text{w}}$.
5. Applying six Dirichlet boundary conditions (BCs) on the whole boundary of the RVE corresponding to homogeneous boundary strains, namely three 1-D axial and three simple shear strains, and solving the corresponding linear elasticity problem using a stationary solver.
6. Postprocessing the results of the FE computations to compute the effective elastic tensor of the RVE, $\mathbb{C}_{\text{cort}}^{\text{FEM}}$.
7. Exporting the results of the FE computations (in particular, the tensor $\mathbb{C}_{\text{cort}}^{\text{FEM}}$) to an Excel spreadsheet.
8. Extracting the relevant elastic moduli from the tensor $\mathbb{C}_{\text{cort}}^{\text{FEM}}$.

3 Results

3.1 Volume fractions

Table 1 shows the experimental mean values (μ_{exp}) and dispersions (δ_{exp}) of HP, TMD, and volume fractions of bone components for individual RVEs (local statistics) and for all the RVEs together (global statistics, last but one row).

The HP of all the RVEs but two is comprised between 4 and 9 %, what is quite usual for cortical bone. In two cases (RVEs ♯9 and ♯10), the HP is unusually high (about 20 and 15 %, respectively). The TMD of each RVEs and the global mean value of TMD are all about 1 g/cm^3. The TMD distributions of RVEs ♯9 and ♯10 do not significantly differ from those of the other RVEs. As reported in Sansalone et al. (2012b), the local TMD slightly decreases in the axial direction when moving from the distal to the proximal part of the sample (i.e. for increasing values of z at fixed values of θ).

The same remarks as for the HP and TMD apply to the volume fraction of the Haversian pores in the tissue ($f_{\text{pore}}^{\text{cort}}$) on the one side and to the volume fractions of the collagen in the ultrastructure ($f_{\text{col}}^{\text{ultra}}$) and of the mineral in the mineral

Table 1 Spatial averages and dispersions of experimental values of HP, TMD, and volume fractions of bone constituents for individual RVEs, the whole ensemble, and the whole ensemble but RVEs ♯9 and ♯10

RVE	(z, θ) (mm, °)	HP		TMD		$f_{\text{pore}}^{\text{cort}}$		$f_{\text{col}}^{\text{ultra}}$		$f_{\text{HA}}^{\text{foam}}$	
		μ_{exp} (%)	δ_{exp} (–)	μ_{exp} (g/cm^3)	δ_{exp} (–)	μ_{exp} (–)	δ_{exp} (–)	μ_{exp} (–)	δ_{exp} (–)	μ_{exp} (–)	δ_{exp} (–)
1	(5.5, −40)	6.47	N/A	0.98	0.0627	0.0647	N/A	0.354	0.0135	0.504	0.0696
2	(3.5, −40)	6.49	N/A	1.02	0.0622	0.0649	N/A	0.357	0.0135	0.528	0.0689
3	(1.5, −40)	4.15	N/A	1.05	0.0543	0.0415	N/A	0.359	0.0117	0.544	0.0601
4	(5.5, −20)	5.26	N/A	0.96	0.0703	0.0526	N/A	0.352	0.0151	0.492	0.0781
5	(3.5, −20)	6.21	N/A	0.98	0.0677	0.0621	N/A	0.354	0.0146	0.508	0.0752
6	(1.5, −20)	8.46	N/A	1.02	0.0649	0.0846	N/A	0.357	0.0139	0.530	0.0719
7	(5.5, 0)	8.80	N/A	0.96	0.0795	0.0880	N/A	0.352	0.0170	0.493	0.0882
8	(3.5, 0)	5.91	N/A	1.00	0.0685	0.0591	N/A	0.355	0.0147	0.516	0.0760
9*	(1.5, 0)	20.7	N/A	1.02	0.0800	0.207	N/A	0.357	0.0138	0.530	0.0708
10*	(5.5, 20)	15.5	N/A	0.98	0.0707	0.155	N/A	0.354	0.0152	0.505	0.0785
11	(3.5, 20)	5.89	N/A	1.03	0.0579	0.0589	N/A	0.358	0.0125	0.534	0.0641
12	(1.5, 20)	7.39	N/A	1.02	0.0649	0.0739	N/A	0.357	0.0138	0.530	0.0719
All		8.44	0.571	1.00	0.0715	0.0844	0.571	0.356	0.0154	0.518	0.0794
All but*		6.50	0.216	1.00	0.0717	0.0650	0.216	0.356	0.0155	0.518	0.0796

Location of RVEs refers to the (z, θ) coordinates described in Sect. 2.1.2. *N/A* not applicable
Asterisks indicate VERs with unusually high HP

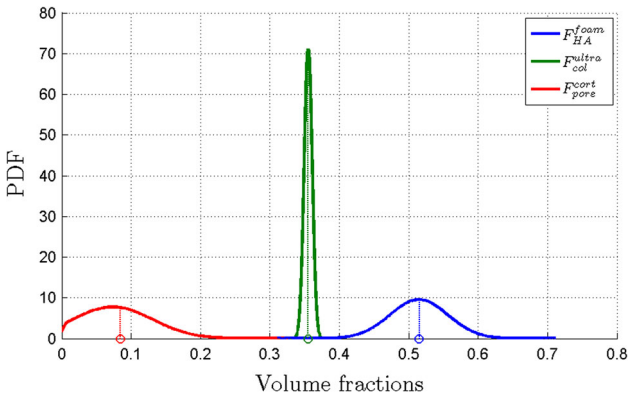

Fig. 5 PDFs of the random volume fractions estimated on the basis of $N = 10^6$ statistically independent realisations. *Red*, *green*, and *blue solid lines* represent the distributions of the statistically independent realisations of $F_{\text{pore}}^{\text{cort}}$, $F_{\text{col}}^{\text{ultra}}$, and $F_{\text{HA}}^{\text{foam}}$, respectively. *Red*, *green*, and *blue knots* and *dotted vertical lines* depict the corresponding mean values

foam ($f_{\text{HA}}^{\text{foam}}$) on the other side. Based on the data reported in Table 1, the standard deviations of the volume fractions (computed with respect to all the 12 RVEs) are: $\sigma_{\text{exp}}(f_{\text{pore}}^{\text{cort}}) = 0.0482$, $\sigma_{\text{exp}}(f_{\text{col}}^{\text{ultra}}) = 0.0055$, and $\sigma_{\text{exp}}(f_{\text{HA}}^{\text{foam}}) = 0.0411$. It can be noticed that the standard deviations of $f_{\text{pore}}^{\text{cort}}$ and $f_{\text{HA}}^{\text{foam}}$ are quite similar although their dispersions are not.

Experimental mean values and dispersions of the volume fractions $f_{\text{pore}}^{\text{cort}}$, $f_{\text{col}}^{\text{ultra}}$, and $f_{\text{HA}}^{\text{foam}}$ in the last but one row of Table 1 (row "All") were used as input data for the probabilistic models of the random volume fractions $F_{\text{pore}}^{\text{cort}}$, $F_{\text{col}}^{\text{ultra}}$, and $F_{\text{HA}}^{\text{foam}}$. A total of $N = 10^6$ statistically independent realisations of each volume fraction were computed.

Approximations of the PDFs of the random volume fractions are shown in Fig. 5. Red, green, and blue lines represent the distributions of the statistically independent realisations of $F_{\text{pore}}^{\text{cort}}$, $F_{\text{col}}^{\text{ultra}}$, and $F_{\text{HA}}^{\text{foam}}$, respectively. Red, green, and blue knots and dotted vertical lines depict the corresponding mean values. The realisations $F_{\text{col}}^{\text{ultra}}(a_i)$ stay very close to the mean value of $F_{\text{col}}^{\text{ultra}}$, while the realisations $F_{\text{pore}}^{\text{cort}}(a_i)$ and $F_{\text{HA}}^{\text{foam}}(a_i)$ spread out, according to the larger values of the standard deviations of $F_{\text{pore}}^{\text{cort}}$ and $F_{\text{HA}}^{\text{foam}}$. Note that the dispersion—the ratio between the standard deviation and the mean value—is a *relative* marker of spreading of data and smaller values of dispersion do not necessarily lead to tighter distributions.

Convergence of the statistical estimators of the mean values (μ_N) and dispersions (δ_N) of the random volume fractions towards the mean values (μ) and dispersions (δ) was assessed. It is worth recalling that statistics of the random volume fractions were set to the experimental statistics in the last but one row of Table 1, that is $\mu = \mu_{\text{exp}}$ and $\delta = \delta_{\text{exp}}$. The magnitudes of the relative errors between experimental statistics (taken as references) and statistical estimators after $N = 10^6$ statistically independent realisations were smaller than 0.1 %. This validated the random generator in Eq. (21) used for constructing the statistically independent realisations of the random volume fractions. The statistical estimators of the mean values and dispersions of the random volume fractions are shown in Fig. 6 as a function of the number n of realisations. Red, green, and blue lines and bars refer to $F_{\text{pore}}^{\text{cort}}$, $F_{\text{col}}^{\text{ultra}}$, and $F_{\text{HA}}^{\text{foam}}$, respectively. Plots in the left and right columns refer to the mean values and dispersions, respectively. On the top, the statistical estimators of the mean values (μ_n) and dispersions (δ_n) of the random volume fractions are depicted by solid lines in semilogarithmic scale. Moreover, the mean values (μ) and dispersions (δ) of the random volume fractions are depicted by dashed lines. As the number of realisations n increases, the statistical estimators (μ_n and δ_n) are computed on larger and larger databases $\{F_{\text{pore}}^{\text{cort}}(a_i)\}_n$, $\{F_{\text{col}}^{\text{ultra}}(a_i)\}_n$, and $\{F_{\text{HA}}^{\text{foam}}(a_i)\}_n$ and converge to the statistics (μ and δ) of the random volume fractions as $n \to N$. On the bottom, the magnitudes of the relative errors of the statistical estimators of the mean values and dispersions, $\text{err}(\mu_n) = |(\mu_n - \mu)/\mu|$ and $\text{err}(\delta_n) = |(\delta_n - \delta)/\delta|$, respectively, are shown in logarithmic scale. Exponential trend lines (dark coloured lines) are also shown. It can be noticed that the relative errors on the mean values and dispersions become smaller than 1 and 0.1 % after 10^4 and 10^5 statistically independent realisations, respectively.

3.2 Elastic moduli

A total of $N' = 10^5$ runs of the multiscale model were performed using the database of volume fractions previously built. The outcome was a database of N' statistically independent realisations of random elastic tensors of the cortical tissue, $\{\mathbb{C}_{\text{cort}}(a_i)\}$, with $i = 1, \ldots, N'$. The nominal elastic tensor of the cortical tissue, $\mathbb{c}_{\text{cort}}^{\mu}$, was also computed. In view of the assumptions made in Sect. 2.2.5, tensors $\mathbb{c}_{\text{cort}}^{\mu}$ and $\{\mathbb{C}_{\text{cort}}(a_i)\}$ turn out to be transversely isotropic, the isotropy plane being the cross section of the femoral neck.

Statistics of the random elastic moduli were computed. The nominal elastic moduli were compared with the mean values of the random moduli to assess the relevance of the nominal model.

In view of the transverse isotropy of $\mathbb{C}_{\text{cort}}$, we focused on the axial moduli in the cross section (Y_1) and along the axis (Y_3) of the femoral neck, the shear moduli in the cross section (G_{12}) and in the sagittal plane ($G_{13} = G_{23}$), and the lateral contraction moduli in the cross section ($V_{12} = V_{21}$) and in the sagittal plane ($V_{13} = V_{23}$), that is the contraction in the cross-sectional plane due to a unit extension in the axial direction. Subscripts $\{1, 2, 3\}$ refer to the Cartesian frame in Fig. 1. Note that axial and lateral contraction moduli correspond to the Young's modulus and Poisson ratio, respectively, for an isotropic material.

Statistics of the random elastic moduli, nominal elastic moduli, and relative differences as in Eq. (29) are reported

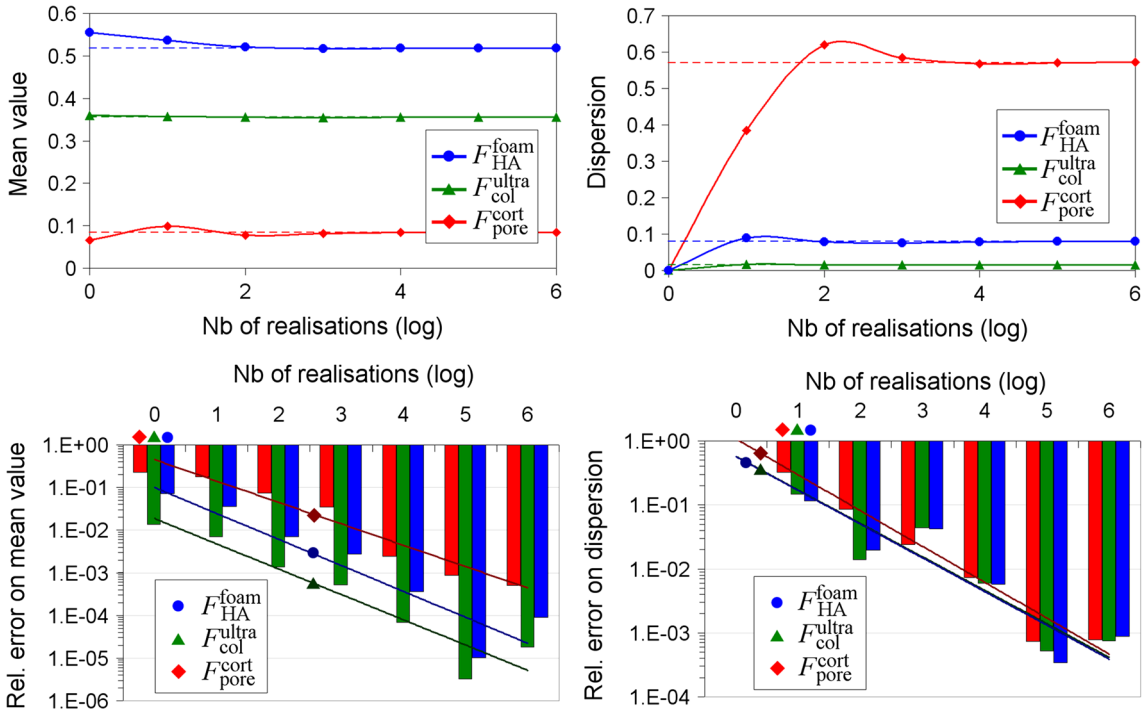

Fig. 6 *Statistics* of the random volume fractions and their *statistical estimators* as a function of the number of realisations. *Red*, *green*, and *blue lines*, *bars*, and *symbols* refer to $F_{\text{pore}}^{\text{cort}}$, $F_{\text{col}}^{\text{ultra}}$, and $F_{\text{HA}}^{\text{foam}}$, respectively. *Diamonds*, *triangles*, and *circles* refer to $F_{\text{pore}}^{\text{cort}}$, $F_{\text{col}}^{\text{ultra}}$, and $F_{\text{HA}}^{\text{foam}}$, respectively. *On the top* Mean values and dispersions (*straight dashed lines*) and their statistical estimators (*solid lines*). *On the bottom* Magnitude of the relative errors of the statistical estimators of the mean values and dispersions. *Dark coloured lines* are exponential trend lines.

Table 2 Statistics of the random moduli, nominal elastic moduli, and their relative differences Eq. (29)

Stochastic model	Y_1 (GPa)	Y_3 (GPa)	G_{12} (GPa)	G_{13} (GPa)	V_{12} (–)	V_{13} (–)
Mean value	5.6416	7.5952	2.0485	2.3228	0.3917	0.2629
SD	2.3751	3.8096	0.8983	1.1055	0.0505	0.0542
Dispersion (–)	0.4210	0.5016	0.4385	0.4759	0.1288	0.2062
2.5 % quantile	1.7007	1.8900	0.5767	0.5968	0.3341	0.1826
25 % quantile	3.9172	4.6905	1.3949	1.5023	0.3643	0.2216
75 % quantile	7.1296	9.9348	2.6044	3.0019	0.4091	0.3000
97.5 % quantile	10.8355	16.2558	4.0361	4.8067	0.4777	0.3742
Nominal model	y_1^μ (GPa)	y_3^μ (GPa)	g_{12}^μ (GPa)	g_{13}^μ (GPa)	v_{12}^μ (–)	v_{13}^μ (–)
	5.4358	7.0657	1.9619	2.1861	0.3854	0.2546
Relative difference Eq. (29)	err(y_1^μ) (%)	err(y_3^μ) (%)	err(g_{12}^μ) (%)	err(g_{13}^μ) (%)	err(v_{12}^μ) (%)	err(v_{13}^μ) (%)
	3.6478	6.9717	4.2281	5.8888	1.6178	3.1668

Random moduli—Y_1, axial modulus in the cross-sectional plane; Y_3, axial modulus along the axis of the femoral neck; G_{12}, shear modulus in the cross section; $G_{13} = G_{23}$, shear modulus in the sagittal plane; $V_{12} = V_{21}$, lateral contraction modulus in the cross section; $V_{13} = V_{23}$, lateral contraction modulus in the sagittal plane (i.e.contraction in the cross-sectional plane due to a unit extension in the axial direction). Subscripts $\{1, 2, 3\}$ refer to the Cartesian frame in Fig. 1. Dispersion values are dimensionless. Nominal moduli and relative differences follow the same notation

in Table 2. The differences between the mean values of the random elastic moduli and the nominal elastic moduli are always smaller than 10 %. Therefore, the deterministic elastic tensor computed through the nominal model provides a quite reasonable approximation of the random elastic tensor computed through the stochastic model. Moreover, leaving aside parallel programming, the computational time required to compute the (deterministic) nominal elastic tensor is N'

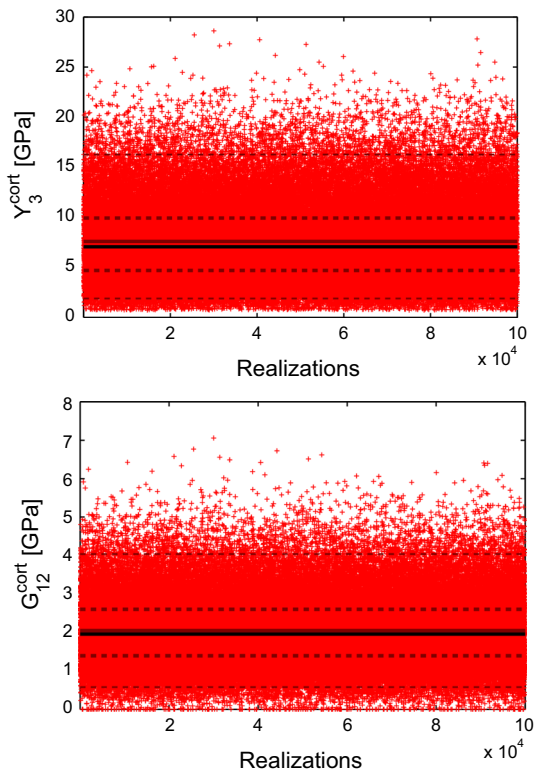

Fig. 7 Axial (*on the top*) and shear (*on the bottom*) elastic moduli along the axis and in the cross section of the femoral neck, that is Y_3 and G_{12}, respectively. *Red crosses* refer to the realisations of the random elastic moduli. *Brown straight lines* refer to the *statistics* of the random elastic moduli. *Solid*, *thick dashed and thin dashed straight brown lines* refer to the mean values, 50 and 95 % confidence intervals of the random moduli, respectively. *Solid black straight lines* refer to the nominal elastic moduli

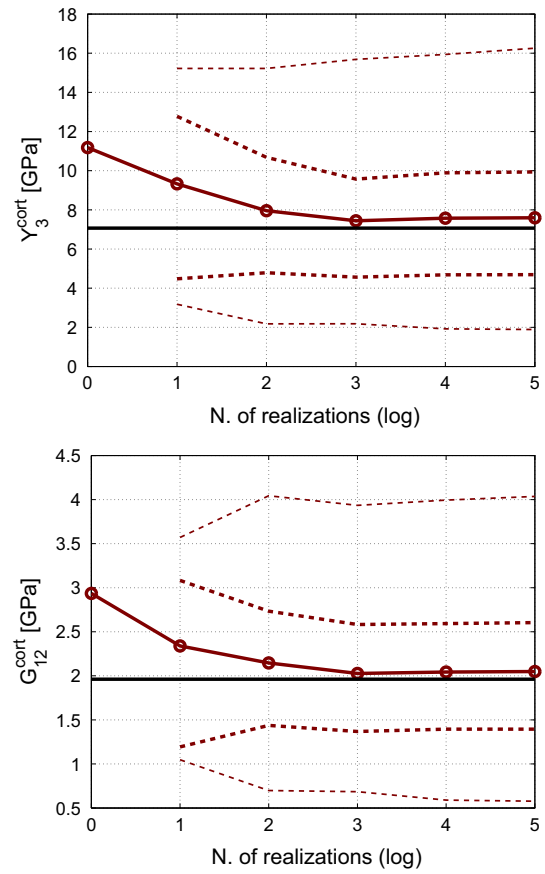

Fig. 8 Axial (*on the top*) and shear (*on the bottom*) moduli along the axis and in the cross section of the femoral neck, that is Y_3 and G_{12}, respectively. *Solid*, *thick dashed and thin dashed brown lines* refer to the *statistical estimators* of the mean values, 50 and 95 % confidence intervals of the random elastic moduli, respectively. *Solid black straight lines* refer to the nominal elastic moduli

orders of magnitude smaller than that required to estimate the random elastic tensor of the stochastic model. (The stochastic model requires additional computational time to store the large amount of data of the N' realisations and compute statistics.)

The axial modulus along the axis (Y_3, on the top) and the shear modulus in the cross-sectional plane (G_{12}, on the bottom) of the femoral neck are shown in Fig. 7. Red crosses refer to the realisations of the random elastic moduli. Straight lines refer to the *statistics* of the random moduli (which do not depend on the realisations) and to the nominal model. Solid, thick dashed and thin dashed brown lines refer to the mean values, 50 and 95 % confidence intervals of the random moduli, respectively. Confidence intervals are plotted based on the quantiles given in Table 2. Solid black lines refer to the nominal elastic moduli.

The statistical estimators of the mean values and confidence intervals of the random elastic moduli Y_3 and G_{12} are presented in Fig. 8 as a function of the number of realisations n. Statistical estimators of the mean values and dispersions of the random elastic moduli converge towards the mean values and dispersions of the random elastic moduli as the number of independent realisations increases ($n \to N'$). (Recall that statistics of the random elastic moduli are set to the statistical estimators computed on $N' = 10^5$ statistically independent realisations.) As for the volume fractions, convergence is almost achieved after $n = 10^4$ statistically independent realisations, the relative errors of the statistical estimators being smaller than a few percent.

In Fig. 9, the estimated PDFs of the realised elastic moduli are presented. Solid, thick dashed and thin dashed brown lines refer to the averages, 50 and 95 % confidence intervals of these random moduli, respectively. Solid black lines refer to the nominal elastic moduli. The PDFs of the random elastic moduli are quite asymmetric and do not show a Gauss-like shape.

Results of the multiscale models were compared with a reference FE model. FE estimates of the elastic tensors, $\mathbb{C}_{cort}^{FEM}(j)$ with $j = 1, \ldots, 12$, were computed for the 12 RVEs identified in Sect. 2.1.2. Unlike elastic tensors $\mathbb{C}_{cort}(a_i)$—which represent fictitious RVEs with idealised pore geometry

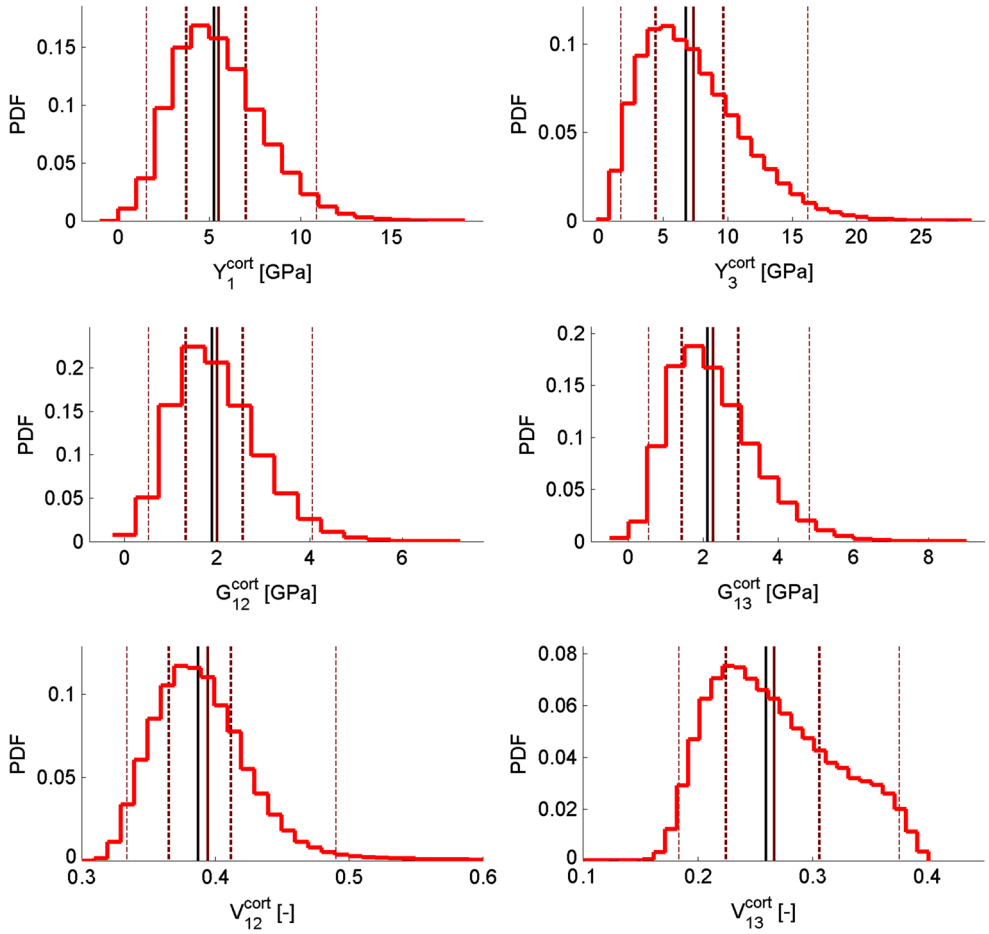

Fig. 9 Approximations of PDFs of the random elastic moduli. *Vertical brown straight lines* refer to the *statistics* of the random elastic moduli. *Solid*, *thick dashed and thin dashed brown lines* refer to the mean values, 50 and 95 % confidence intervals of these random moduli, respectively. *Solid black straight lines* refer to the nominal elastic moduli (Colors in online version.)

and homogeneous ultrastructure, each FE tensor $\mathbb{c}_{\text{cort}}^{\text{FEM}}(j)$ accounts for the specific Haversian pore geometry and heterogeneous ultrastructure of one actual RVE. Therefore, tensors $\mathbb{c}_{\text{cort}}^{\text{FEM}}(j)$ should be regarded as references for the multiscale model to be compared with. First of all, the accuracy of the multiscale model was assessed for the 12 RVEs. The homogenised elastic tensor of each RVE was computed using the deterministic, homogenised model presented in Sect. 2.2.1 and taking the HP and mean value of TMD of the RVE (see Table 1) as input data. The deterministic, homogenised model provided results very similar to those of the FEM model. The relative differences of the Frobenius norms of the homogenised and FE elastic tensors were smaller than a few percent for all the 12 RVEs (data not shown).

Comparison between the stochastic model, the nominal model, and the FE model is shown in Fig. 10. Results of the FE model are represented by blue circles in Fig. 10. Solid, dashed and dotted brown lines refer to the averages, 95 and 50 % confidence intervals of the random moduli, respectively. Solid black lines refer to the nominal elastic moduli. The elastic moduli of all the 12 RVEs were found to fall within the 95 % confidence interval of the stochastic model. Moreover, most of these elastic moduli were found to fall within the 50 % confidence interval of the stochastic model. Three RVEs show some elastic moduli falling out of the 50 % confidence interval, namely RVEs ♯3, ♯9, and ♯10. These RVEs are characterised by lowest (RVE ♯3) and highest (RVEs ♯9 and ♯10) values of HP, leading to highest and lowest elastic moduli, respectively.

4 Discussion

Multiscale modelling and simulation are powerful methods to predict bone mechanical properties as long as information on bone organisation and composition at different structural scales is available. Experimental information on microstructural features can be accounted for in multiscale models and FE simulations (Bourne and van der Meulen 2004; Hellmich

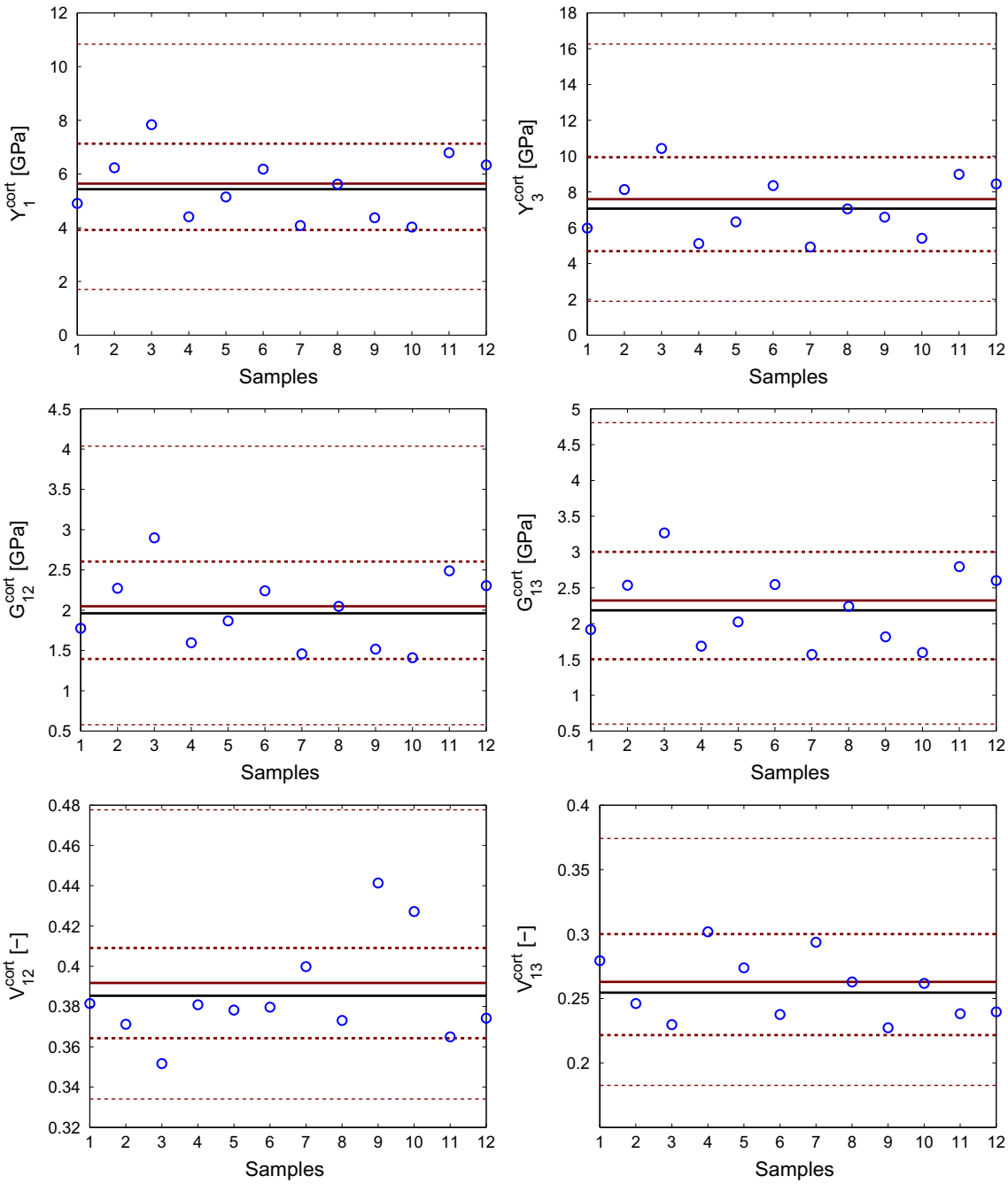

Fig. 10 Comparison between the elastic moduli of the actual RVEs and the *statistics* of the random elastic moduli. *Blue circles* refer to the 12 RVEs in Table 1. *Solid*, *thick dashed and thin dashed brown lines* refer to the mean values, 50 and 95 % confidence intervals of the random moduli, respectively. *Solid black straight lines* refer to the nominal elastic moduli

et al. 2008; Sansalone et al. 2010, 2012b; Wagner et al. 2011; Blanchard et al. 2013; Graeff et al. 2013; Sreenivasan et al. 2013). In particular, HP and mineral content of bone matrix (TMD) are known to relate with the mechanical properties of bone (Burr 2004). Information on HP and TMD can be provided by experimental measurements at the relevant scales, i.e. a few hundreds micrometres and several micrometres for the HP and TMD, respectively. X-Ray-based devices are commonly used in scientific research and clinical practice to probe bone microstructure. Advanced imaging techniques as SR-μCT can provide quite accurate information on bone microstructure at the micrometric scale or even below (Nuzzo et al. 2002; Bousson et al. 2004) but are limited to *in vitro* studies on small human bone samples. Medical

devices currently used in clinical practice, such as DXA devices or QCT scans, have much coarser spatial resolution (typically one mm to several hundreds μm) and cannot provide as much accurate information. More recently, improved 3-D imaging techniques have been introduced such as μ-CT, high-resolution peripheral quantitative μ-CT (HR-pQCT), and multidetector CT (MDCT) (Burghardt et al. 2011). These techniques allow imaging bone in vivo with spatial resolution ranging from a few to several hundreds micrometres. Last-generation μCTs allow ex vivo examinations of human specimens as big as entire vertebrae, with spatial resolutions in the 10 μm range, which opens a new way for looking at entire bones in 3-D (Perilli et al. 2012). However, technical limitations related to image quality, radiation dose considerations, and subject motion make it hard to obtain accurate information on HP and TMD through these techniques in in vivo conditions. Technology is rapidly evolving in the field of medical imaging, and improvements can be expected in next years or decades. However, at the present, in vivo medical images turn out to be too much blurred for extracting accurate information on bone microstructure. Uncertainties affecting available in vivo information on bone microstructure may question the reliability of results obtained by multiscale models using these data as entry (Valente et al. 2014). As long as input data are uncertain, deterministic approaches may become unreliable and new modelling paradigms are required.

4.1 The multiscale model: a compromise between accuracy and simplicity

The multiscale description of bone used in this study was developed in order to achieve a good compromise between accuracy (in the predicted elastic coefficients) and simplicity (required by the limited available experimental information). Both nominal and stochastic multiscale models use continuum micromechanics theory and rely on the same assumptions in terms of microstructural organisation of bone at the different scales (mineral foam, ultrastructure, cortical tissue). Limitations related to these assumptions as well as experimental validation have been discussed in previous studies (Sansalone et al. 2010, 2012b). Some of this hypothesis have been investigated by other authors by comparing model predictions with experimental values.

Direct comparison with experimental data is not possible. On the one side, we were not able to perform mechanical testing. On the other side, comparison with data available in literature is tricky since elastic moduli strongly depend on microstructural features (namely the TMD) which we could not find in the literature.

RVE size A cornerstone of any homogenisation model is the concept of RVE. The size of our RVE was chosen looking at the dependency of the elastic coefficients of the cortical tissue—as predicted by the nominal model—on the RVE size (data not shown). It was found that the minimum RVE size should be about half a millimetre. This value is coherent with the findings of other authors (Grimal et al. 2011a) who have addressed this issue using different approaches. Moreover, within the RVE, our model assumes homogeneous material properties around the pores at the tissue scale. This assumption is supported by acoustic measures which revealed a small variation of elastic properties of bone matrix at the millimetre scale (Granke et al. 2011).

Microarchitecture Both Haversian pores (at the tissue scale) and collagen (at the ultrastructural scale) were assumed to be of cylindrical shape and aligned with the femoral neck axis. However, Haversian pores have a more complex geometry (see Fig. 2) and collagen orientation changes from one lamella to another (Reisinger et al. 2011; Spiesz et al. 2011; Granke et al. 2013). Moreover, mineral particles (at the mineral foam scale) were assumed to be spherical whereas they are actually platelets with thickness of a few nanometres and length and width of a few to several tens of nanometres (Rho et al. 1998; Deuerling et al. 2009). While on the one hand our hypothesis of cylindrical pores at the tissue scale seems reasonable (Granke et al. 2015), our assumptions at the lower scales (aligned collagen fibres and spherical mineral particles) may lead to inaccurate predictions (Deuerling et al. 2009). Other micro- and nanoscale features such as the morphology of the lacuno-canalicular network and the mineralisation at the nanoscale can affect bone elasticity, strength, and failure (Tai et al. 2008; Langer et al. 2012; Schrof et al. 2014). All these microarchitectural features should be investigated and their effects on the tissue level properties assessed.

How many scales? The usefulness of a detailed description of bone micro- and nanostructure below the tissue scale is a matter of debate. Our model considers three microstructural levels below the organ and lies in between two families of approaches. On the one side, some authors used very detailed descriptions of bone hierarchical structure (Yoon and Cowin 2008a, b; Fritsch and Hellmich 2007) which fit quite well with experimental measures at different microstructural scales. However, these approaches need experimental input data which are hardly available in a subject-specific study. Other authors suggested that simpler models, basically based on the porosity at the tissue level (Dong and Guo 2006; Granke et al. 2011, 2015), could be enough to catch the main elastic properties of bone. In this case, some discrepancies between experimental measures and model predictions were observed which could be attributed to variations in the elastic properties of microstructural features of bone (Dong and Guo 2006; Granke et al. 2015). This interpretation is coherent with our findings (e.g. RVEs n. 1 and 2 which have quite similar HP and different TMD, see Table 1).

4.2 The stochastic multiscale model: a comprehensive description of bone

The *first goal* of this work was to develop a modelling strategy taking into account the uncertain composition of bone. To this aim, a stochastic multiscale model of cortical bone was developed. To the best of our knowledge, this is the first attempt to compute the elastic properties of cortical bone taking into account simultaneously its multiscale structure *and* the experimental uncertainty on the amount of its elementary components. The deterministic multiscale model of Sansalone et al. (2010, 2012b) was extended in a stochastic framework by treating the volume fractions of bone components as random variables. The non-Gaussian probabilistic models of the volume fractions were obtained using the MaxEnt principle. The experimental information needed to construct the PDFs of the volume fractions was obtained through high-resolution SR-μCT images of the inferior part of a human femoral neck sample. Image analysis of several RVEs in the cortical part of the sample allowed computing the mean value and dispersion of each volume fraction. The stochastic multiscale model was used to quantify the uncertainties relative to the random elastic tensor of cortical tissue and its mean value. Statistics of random elastic moduli (mean value, standard deviation, confidence interval, etc.) were compared with the nominal elastic moduli on the one side and with detailed FE models of the RVEs on the other side.

The stochastic model turns out to provide a reliable representation of the elastic properties of cortical tissue. All the FE results fall within the 90 % confidence interval of the stochastic model. Moreover, all the FE results fall within the 50 % confidence interval of the stochastic model but a few exceptions (three RVEs out of 12, characterised by an unusually high or low HP), see Fig. 10. It should be noted that the outcome of the stochastic model has to be regarded in statistical terms. As long as bone composition at a given anatomical location is known in statistical terms (e.g. average and dispersion), it provides reliable information about the expected value of the local elastic properties and the confidence interval of that estimate. One might expect the elastic moduli of roughly half of the actual RVEs to fall within the 50 % confidence interval of the stochastic model. However, this latter seems to provide a much safer envelop. Figure 10 shows that between 75 and 100 % of the actual RVEs fall within the 50 % confidence interval. This might be due to the information introduced in the MaxEnt principle. This information would lead to PDFs of the *random* volume fractions which are more spread out than those of the *actual* volume fractions. On the one side, some information might be missing: for instance, the bounds 0 and 1 could be considered as repulsive values. On the other side, estimates of mean value and dispersion of random volume fractions could be improved: for instance, instead of considering them as experimentally known values, they could be computed by solving an optimisation problem based on the *maximum likelihood principle*.

4.3 The nominal model: a simple and accurate estimate of expected elastic moduli

The *second goal* of this paper was to identify whether a simpler model exists providing results comparable to those of the stochastic multiscale model. Indeed, while providing a comprehensive representation of bone elasticity, the stochastic model presents some drawbacks which may prevent its direct application for end-user clinical purposes. First of all, the stochastic model requires a high computational time. In this study, the computational time on a standard desktop computer was about half an hour to generate the database of $N = 10^6$ volume fractions and half a day to perform $N' = 10^5$ runs of the three-step homogenisation procedure. Despite this time being quite reasonable for research purposes, it might be not for end-user clinical purposes. Parallelising the computer code would reduce the computational cost. (Roughly speaking, computational time would be divided by the number of parallel processors.) However, this is not worth considering in clinical practice. Moreover, the stochastic model requires *both* the mean values *and* the dispersions of the volume fractions to be estimated, which might not be straightforward. Therefore, the interest for a faster and simpler model is apparent. A candidate meeting these requirements is the *nominal model* introduced in Sect. 2.2.4. The nominal model only needs the mean values of the volume fractions as input data and provides run-time results. Nominal elastic moduli stay quite close to the mean values of the random elastic moduli, with differences of a few per cent, see Table 2. As long as errors smaller than 10 % are acceptable, the nominal model provides a "good" estimate of expected bone elastic moduli. However, it should be reminded that the nominal model is intrinsically unable to provide information about the reliability of these estimates—a shortcoming of any deterministic approach.

4.4 Whole bone: heterogeneity versus homogeneity

Another shortcoming of the nominal model lies in the fact that it cannot account for the heterogeneity of bone at the organ scale. Our experimental data cover the whole cortical region. Then, one should be allowed to use these data to analyse the whole cortical region. The stochastic model would use these data (namely, the mean values and dispersions of the bone volume fractions) to generate a random distribution of elastic tensors at each point of the bone cortex. This result should be regarded in a statistical sense: the spatial distribution of elastic tensors generated by the stochastic model will be sta-

tistically equivalent to the spatial distribution of actual elastic tensors.

Both HP and TMD—and therefore elastic properties—of bone tissue are heterogeneously distributed at the organ scale. The stochastic model could be used to generate a heterogeneous distribution of elastic properties statistically equivalent to the actual one and therefore to set up a FE analysis at the organ scale. The elastic properties of each FE meshing the bone could be randomly generated by the stochastic model. In general, the randomly generated elastic properties of each FE will be different from the actual ones (which are related to the local values of HP and TMD). However, the spatial distributions of randomly generated and actual elastic tensors will be statistically equivalent. In other words, one would obtain the same macroscopic results (such as maximum displacement or limit load) from FE meshes with either heterogeneous randomly generated elastic properties or heterogeneous actual elastic properties.

By contrast, the nominal model would predict the same elastic response at each point of the bone. Using the nominal model to set up, a FE analysis of the whole bone would lead to homogeneous material properties everywhere in the mesh. Is this simplification acceptable? Figure 10 shows that the values of the elastic moduli of individual RVEs obtained through the FE model can be quite different from the elastic moduli predicted by the nominal model (as well as the mean values of the stochastic model), the relative errors approaching 50 % in some cases. The average errors on the axial and shear moduli are about 20 %, and those on the lateral contraction moduli are slightly smaller than 10 %. Indeed, bone turns out to be highly heterogeneous at the organ scale, and the elastic properties can vary considerably within a distance of a few millimetres (as in the bone sample considered in this study), see e.g. the axial modulus along the femoral neck axis of RVEs ♯10 ($z = 5.5\,\text{mm}$, $\theta = 20°$, $y_3^{\text{FEM}} \simeq 5\,\text{GPa}$) and ♯11 ($z = 3.5\,\text{mm}$, $\theta = 20°$, $y_3^{\text{FEM}} \simeq 9\,\text{GPa}$). Therefore, attention should be paid in considering bone as homogeneous at the organ scale.

4.5 Limitations and future research directions

To conclude, a few remarks on the scope and limitations of the proposed modelling strategy are in order. Some limitations of our study are related to the multiscale description of bone and the associated modelling choices. Some of these issues were addressed in Sect. 4.1 and thoroughly discussed in previous work (Sansalone et al. 2010, 2012b). Other limitations are more closely related to the stochastic treatment of modelling variables and will be discussed here below.

Statistical population First of all, only 12 RVEs were considered in this study. This makes largely unreliable the values of the experimental (global) statistics of $f_{\text{pore}}^{\text{cort}}$. A larger number of RVEs should be used to improve accuracy and reliability of the experimental statistics of $f_{\text{pore}}^{\text{cort}}$. For instance, the global mean value of HP is higher than 8 % and its global dispersion is higher than 0.5—a quite high value corresponding to a standard deviation of almost 5 %. Such high values of the global mean value and dispersion are mainly due to the contribution of RVEs ♯9 and ♯10. Excluding these RVEs from the statistical analysis (last row), the global mean value of HP drops to 6.5 % and its global dispersion to 0.2 (corresponding to a standard deviation of 1.4 %). By contrast, experimental statistics on $f_{\text{col}}^{\text{ultra}}$ and $f_{\text{HA}}^{\text{foam}}$ are computed on large numbers of voxel-wise values ($N_{\text{vox}}^{i} \sim 10^5$ and $N_{\text{vox}} > 10^6$ for local and global statistics, respectively). Therefore, no significant errors are expected on those statistics. It should also be noted that this study considered just one bone sample from one anatomical site of one donor. Different results may be obtained for different anatomical sites or donors of different ages or pathological conditions. A longitudinal and cross-sectional study is needed in order to assess the suitability of this approach and the conclusions of this study on different statistical populations.

Statistical independence Experimental volume fractions $f_{\text{HA}}^{\text{foam}}$, $f_{\text{col}}^{\text{ultra}}$, and $f_{\text{pore}}^{\text{cort}}$ are computed based on two pieces of experimental information (HP and TMD), see Sect. 2.2.5. Experimental statistics of $f_{\text{HA}}^{\text{foam}}$, $f_{\text{col}}^{\text{ultra}}$, and $f_{\text{pore}}^{\text{cort}}$ fed the stochastic models of the random volume fractions $F_{\text{HA}}^{\text{foam}}$, $F_{\text{col}}^{\text{ultra}}$, and $F_{\text{pore}}^{\text{cort}}$, respectively, which were considered as statistically independent. Nevertheless, statistical dependence may exist between these random variables. In order to take statistical dependence into account in the MaxEnt principle, objective information is needed. This information could be provided by analysing the dependence (e.g. correlation) possibly existing between the experimental variables. This issue was not investigated yet. Therefore, statistical independence remains a safe hypothesis in the framework of the MaxEnt principle.

Random variables versus random fields Volume fractions are modelled as random variables without spatial correlation. Should this model be used to generate a FE mesh at the organ scale, no relationship would exist between the elastic properties of adjacent points. This is largely unrealistic. As previous studies have shown, elastic moduli in the femoral neck are not only heterogeneous—as already underlined—but also show a global tendency to decrease radially from the periosteum inwards (Sansalone et al. 2010, 2012a) and axially from the distal to the proximal part of the femoral neck (Sansalone et al. 2012b). These variations have been shown to be related to the anatomical variations of HP—increasing from the periosteum inward—and TMD—decreasing from the distal to the proximal part. Moreover, at each point of the femoral neck, the values of HP and TMD may correlate, which would induce dependency between the volume frac-

tions. All these features should be taken into account in the stochastic model of volume fractions and are addressed in a forthcoming work.

Random elastic properties and microarchitecture Moreover, only the volume fractions were considered as random parameters. Both elastic properties and geometric organisation of bone components were fixed to some reference values. However, aiming at patient-specific modelling, modelling of both these features needs to be improved and included in a comprehensive model where all the parameters are described according to the available information. On the one side, elastic coefficients of bone components were already modelled as random variables in previous work (Sansalone et al. 2014). Randomness in the values of the elastic coefficients accounts for the imperfect knowledge of the effective elastic behaviour of bone components at the nanoscale. In that work, all the bone components were considered as elastically isotropic. For sake of coherency, we made the same assumption in this work. However, at the least collagen should be considered transversely isotropic (Hellmich et al. 2004a)—as already done in previous work of our group (Sansalone et al. 2010). On the other side, the idealised microarchitecture assumed in this study should be revisited to comply with a more realistic description. Again, a stochastic treatment might be useful to account for the limited data available on bone microarchitecture.

Validation Furthermore, the stochastic model needs to be validated at the organ scale. At the present, only a numerical validation was performed for each RVE (data not shown). The stochastic model is expected to produce an accurate description of the overall elastic response at the organ scale. Experimental or detailed numerical results at the organ scale are required to prove the reliability of model predictions.

In vivo experimental data Eventually, this study was based on high-resolution SR-μCT images which allowed obtaining a detailed description of bone microstructure and accurate statistical information on HP and TMD in a small bone sample. Aiming at translating this approach to in vivo conditions, some critical issues arise concerning the experimental data. On the one side, the physics of imaging (for instance, dose in X-ray CT) limits the spatial resolution of clinical CT scanners. Peripheral CT scans can achieve a spatial resolution of about 80 μm. However, the spatial resolution of clinical scanners for imaging spine and hip is of several hundreds of micrometres, which is inadequate for highly accurate cortical measurements (Genant and Jiang 1068). On the other side, clinical applications cannot be restricted to small anatomical sites as in this study. Imaging whole organs (or large parts of them) with a resolution of several micrometres requires managing very big data. Nowadays, the need for accurate measurements at the microstructural scale on whole bones constitutes a critical bottleneck for the approach proposed in this paper to be transferred to clinical practice. In order to overcome this difficulty, a robust protocol is necessary to retrieve statistical information at the finer scales—required by the model—from measurements at the coarser scales—typical of medical devices. The improvement of imaging resolution would become nonessential if useful information from bone microarchitecture, such as heterogeneity of spatial mineral distribution, can be extracted from the low-resolution images. Several multimodal studies exist which compare and correlate experimental data coming from different imaging techniques (Grampp et al. 1997; Heilmann et al. 1998; Rossini et al. 1998; Genant et al. 2000; Apostol et al. 2006; Bagi et al. 2006; Chappard et al. 2006; Engelke et al. 2009; Guglielmi et al. 2011; Ito 2000; Nishiyama and Boyd 2011; Link 2012; Baum et al. 2013; Lewiecki 2013). These studies point out the difficulty to retrieve accurate microstructural information from 2-D or 3-D medical devices. Recently, a stochastic approach was proposed to examine 2-D DXA images and quantitatively assess the heterogeneity of spatial mineral distribution (Dong and Wang 2013) opening the way to further studies in this direction.

5 Conclusion

Lack of patient-specific data and uncertainties affecting available information on bone microstructure, especially in vivo and at the small scales of its hierarchical structure, may question the reliability of results provided by models based on these experimental input data. In order to overcome these difficulties, we proposed in this paper a novel modelling approach taking into account *both* the hierarchical structure of bone *and* the uncertainty existing on the experimental data. The hierarchical structure of bone is accounted for using a continuum micromechanics approach. Uncertain experimental data are treated as random variables, and their probability distributions are built using the MaxEnt principle. The outcome is a stochastic multiscale model which uses statistics (mean and dispersion) on experimental measures of bone composition to provide statistics (mean, dispersion, confidence intervals, etc.) on the elastic properties of the cortical tissue. The stochastic multiscale model was validated against detailed FE calculations and proved to describe correctly the heterogeneous elastic properties of cortical tissue at the organ scale. A simpler nominal multiscale model was also proposed which may be useful when heterogeneity can be neglected. Experimental input data of this study were provided by SR-μCT images of a femoral neck sample. These images provided detailed statistics on bone composition which were used for both the stochastic multiscale model and the FE analysis. This work is a first step in patient-specific modelling, and several limitations exist which will

be addressed in future work. Some limitations are related to the modelling (spatial correlation of experimental data and uncertainty on the microarchitecture are not accounted for) and others to the technology of the clinical devices which, at present, cannot provide the experimental data required by the model.

References

Aoubiza B, Crolet JM, Meunier A (1996) On the mechanical characterization of compact bone structure using the homogenization theory. J Biomech 29(12):1539–1547

Apostol L, Boudousq V, Basset O, Odet C, Yot S, Tabary J, Dinten JM, Boiler E, Kotzki PO, Peyrin F (2006) Relevance of 2D radiographic texture analysis for the assessment of 3D bone micro-architecture. Med Phys 33(9):3546–3556

Arnold L (1973) Stochastic differential equations: theory and applications. Wiley, New York

Bagi CM, Hanson N, Andresen C, Pero R, Lariviere R, Turner CH, Laib A (2006) The use of micro-CT to evaluate cortical bone geometry and strength in nude rats: correlation with mechanical testing, pQCT and DXA. Bone 38(1):136–144

Basaruddin KS, Takano N, Nakano T (2015) Stochastic multi-scale prediction on the apparent elastic moduli of trabecular bone considering uncertainties of biological apatite (BAp) crystallite orientation and image-based modelling. Comput Methods Biomech Biomed Eng 18(2):162–174

Baum T, Karampinos DC, Liebl H, Rummeny EJ, Waldt S, Bauer JS (2013) High-resolution bone imaging for osteoporosis diagnostics and therapy monitoring using clinical MDCT and MRI. Curr Med Chem 20(38):4844–4852

Bell KL, Loveridge N, Power J, Garrahan N, Meggitt BF, Reeve J (1999) Regional differences in cortical porosity in the fractured femoral neck. Bone 24(1):57–64

Bensamoun S, Gherbezza J-M, de Belleval J-F, Ho Ba Tho M-C (2004a) Transmission scanning acoustic imaging of human cortical bone and relation with the microstructure. Clin Biomech 19:639–647

Bensamoun S, Ho Ba Tho M-C, Luu S, Gherbezza J-M, de Belleval J-F (2004b) Spatial distribution of acoustic and elastic properties of human femoral cortical bone. J Biomech 37:503–510

Blanchard R, Dejaco A, Bongaers E, Hellmich C (2013) Intravoxel bone micromechanics for microCT-based finite element simulations. J Biomech 46(15):2710–2721

Boivin G, Meunier PJ (2002) The degree of mineralization of bone tissue measured by computerized quantitative contact microradiography. Calcif Tissue Int 70(6):503–511

Bourne BC, van der Meulen MC (2004) Finite element models predict cancellous apparent modulus when tissue modulus is scaled from specimen CT-attenuation. J Biomech 37(5):613–621

Bousson V, Meunier A, Bergot C, Vicaut E, Rocha MA, Morais MH, Laval-Jeantet AM, Laredo JD (2001) Distribution of intracortical porosity in human midfemoral cortex by age and gender. J Bone Miner Res 16(7):1308–1317

Bousson V, Peyrin F, Bergot C, Hausard M, Sautet A, Laredo JD (2004) Cortical bone in the human femoral neck: three-dimensional appearance and porosity using synchrotron radiation. J Bone Miner Res 19(5):794–801

Bouxsein ML (2003) Bone quality: Where do we go from here? Osteoporos Int 14(S5):S118–S127

Bouxsein ML, Boyd SK, Christiansen BA, Guldberg RE, Jepsen KJ, Mller R (2010) Guidelines for assessment of bone microstructure in rodents using micro-computed tomography. J Bone Miner Res 25(7):1468–1486

Broz JJ, Simske SJ, Greenberg AR (1995) Material and compositional properties of selectively demineralised cortical bone. J Biomech 28(11):1357–1368

Burghardt AJ, Link TM, Majumdar S (2011) High-resolution computed tomography for clinical imaging of bone microarchitecture. Clin Orthop Relat Res 469(8):2179–2193

Burr DB (2004) Bone quality: understanding what matters. J Musculoskelet Neuronal Interact 4(2):184–186

Chappard C, Basillais A, Benhamou L, Bonassie A, Brunet-Imbault B, Bonnet N, Peyrin F (2006) Comparison of synchrotron radiation and conventional X-ray microcomputed tomography for assessing trabecular bone microarchitecture of human femoral heads. Med Phys 33(9):3568–3577

Crabtree N, Loveridge N, Parker M, Rushton N, Power J, Bell KL, Beck TJ, Reeve J (2001) Intracapsular hip fracture and the region-specific loss of cortical bone: analysis by peripheral quantitative computed tomography. J Bone Miner Res 16(7):1318–1328

Currey JD (1988) The effect of porosity and mineral content on the young's modulus of elasticity of compact bone. J Biomech 21(2):131–139

Deuerling JM, Yue W, Espinoza Orías AA, Roeder RK (2009) Specimen-specific multi-scale model for the anisotropic elastic constants of human cortical bone. J Biomech 42(13):2061–2067

Devroye L (1986) Non uniform random variate generation. Springer, New York

Dong X, Guo XE (2006) Prediction of cortical bone elastic constants by a two-level micromechanical model using a generalized self-consistent method. J Biomech Eng 128(3):309–316

Dong X, Wang X (2013) Assessment of bone fragility with clinical imaging modalities. Hard Tissue 2(1):7

Donnelly E (2011) Methods for assessing bone quality: a review. Clin Orthop Relat Res 469(8):2128–2138

Engelke K, Libanati C, Liu Y, Wang H, Austin M, Fuerst T, Stampa B, Timm W, Genant HK (2009) Quantitative computed tomography (QCT) of the forearm using general purpose spiral whole-body ct scanners: accuracy, precision and comparison with dual-energy X-ray absorptiometry (DXA). Bone 45(1):110–118

Eshelby J (1957) The determination of the elastic field of an ellipsoidal inclusion, and related problems. Proc R Soc Lond Ser A 241:376–396

Feller W (1971) An introduction to probability theory and its applications. Wiley, New York

Fratzl P, Gupta HS, Paschalis EP, Roschger P (2004) Structure and mechanical quality of the collagenmineral nano-composite in bone. J Mater Chem 14:2115–2123

Fritsch A, Hellmich C (2007) 'Universal' microstructural patterns in cortical and trabecular, extracellular and extravascular bone materials: Micromechanics-based prediction of anisotropic elasticity. J Theor Biol 244(4):597–620

Genant HK, Jiang Y (1068) Advanced imaging assessment of bone quality. Ann N Y Acad Sci 410–428:2006

Genant HK, Gordon C, Jiang Y, Link TM, Hans D, Majumdar S, Lang TF (2000) Advanced imaging of the macrostructure and microstructure of bone. Horm Res Paediatr 54(S1):24–30

Ghanbaria J, Naghdabadi R (2009) Nonlinear hierarchical multiscale modeling of cortical bone considering its nanoscale microstructure. J Biomech 42(10):1560–1565

Graeff C, Marin F, Petto H, Kayser O, Reisinger A, Peña J, Zysset P, Glüer CC (2013) High resolution quantitative computed tomography-based assessment of trabecular microstructure and strength estimates by finite-element analysis of the spine, but not dxa, reflects vertebral fracture status in men with glucocorticoid-induced osteoporosis. Bone 52(2):568–577

Grampp S, Genant HK, Mathur A, Lang P, Jergas M, Takada M, Glüer CC, Lu Y, Chavez M (1997) Comparisons of noninvasive bone mineral measurements in assessing age-related loss, fracture

discrimination, and diagnostic classification. J Bone Miner Res 12(5):697–711
Granke M, Grimal Q, Saïed A, Nauleau P, Peyrin F, Laugier P (2011) Change in porosity is the major determinant of the variation of cortical bone elasticity at the millimeter scale in aged women. Bone 49(5):1020–1026
Granke M, Gourrier A, Rupin F, Raum K, Peyrin F, Burghammer M, Saïed A, Laugier P (2013) Microfibril orientation dominates the microelastic properties of human bone tissue at the lamellar length scale. PLoS One 8(3):e58043
Granke M, Grimal Q, Parnell WJ, Raum K, Gerisch A, Peyrin F, Saïed A, Laugier P (2015) To what extent can cortical bone millimeter-scale elasticity be predicted by a two-phase composite model with variable porosity? Acta Biomater 12:207–215
Grimal Q, Raum K, Gerisch A, Laugier P (2011a) A determination of the minimum sizes of representative volume elements for the prediction of cortical bone elastic properties. Biomech Model Mechanobiol 10:925–937
Grimal Q, Rus G, Parnell WJ, Laugier P (2011b) A two-parameter model of the effective elastic tensor for cortical bone. J Biomech 44(8):1621–1625
Grimal Q, Rohrbach D, Grondin J, Barkmann R, Glüer CC, Raum K, Laugier P (2014) Modeling of femoral neck cortical bone for the numerical simulation of ultrasound propagation. Ultrasound Med Biol 40(5):1015–1026
Guglielmi G, Muscarella S, Bazzocchi A (2011) Integrated imaging approach to osteoporosis: state-of-the-art review and update. Radiographics 31(5):1343–1364
Guilleminot J, Soize C (2012) Probabilistic modeling of apparent tensors in elastostatics: a maxent approach under material symmetry and stochastic boundedness constraints. Probab Eng Mech 28(SI):118–124
Guilleminot J, Soize C (2013a) On the statistical dependence for the components of random elasticity tensors exhibiting material symmetry properties. J Elast 111(2):109–130
Guilleminot J, Soize C (2013b) tochastic model and generator for random fields with symmetry properties: application to the mesoscopic modeling of elastic random media. Multiscale Model Simul 11(3):840–870
Guilleminot J, Noshadravan A, Soize C, Ghanem RG (2011) A probabilistic model for bounded elasticity tensor random fields with application to polycrystalline microstructures. Comput Methods Appl Mech Eng 200(17–20):1637–1648
Haiat G, Naili S, Grimal Q, Talmant M, Desceliers C, Soize C (2009) Influence of a gradient of material properties on ultrasonic wave propagation in cortical bone: Application to axial transmission. J Acoust Soc Am 125(6):4043–4052
Haiat G, Naili S, Vu M-B, Desceliers C, Soize C (2011) Equivalent contributing depth investigated by a lateral wave with axial transmission in heterogeneous viscoelastic cortical bone. J Acoust Soc Am 129(4):EL114–EL120
Halmos P (1976) Measure theory, volume 1: basics, 2nd edn. Springer, Berlin
Heilmann P, Wüster C, Prolingheuer C, Götz M, Ziegler R (1998) Measurement of forearm bone mineral density: comparison of precision of five different instruments. Calcif Tissue Int 62(2):383–387
Hellmich C, Barthelemy J, Dormieux L (2004a) Mineral-collagen interactions in elasticity of bone ultrastructure—a continuum micromechanics approach. Eur J Mech A Solids 23:783–810
Hellmich C, Ulm F-J, Dormieux L (2004b) Can the diverse elastic properties of trabecular and cortical bone be attributed to only a few tissue-independent phase properties and their interactions? Biomech Model Mechanobiol 2:219–238
Hellmich C, Kober C, Erdmann B (2008) Micromechanics-based conversion of CT data into anisotropic elasticity tensors, applied to FE simulations of a mandible. Ann Biomed Eng 23:783–810
Hulmes DJ (2002) Building collagen molecules, fibrils, and suprafibrillar structures. J Struct Biol 137:2–10
Ito M (2000) Recent progress in bone imaging for osteoporosis research. J Bone Miner Metab 29(2):131–140
Jaynes ET (1957a) Information theory and statistical mechanics. Phys Rev 106(4):620–630
Jaynes ET (1957b) Information theory and statistical mechanics. Phys Rev 108(2):171–190
Jumarie G (2000) Maximum entropy. Information without probability and complex fractals. Kluwer Academic Publishers, Dordrecht
Kapur JN, Kesavan HK (1992) Entropy optimization principles with applications. Academic Press, San Diego
Knuth DE (1981) The art of computer programming. Seminumerical algorithms, vol 2. Addison-Wesley, Boston
Kotha SP, Guzelsu N (2000) The effects of interphase and bonding on the elastic modulus of bone: changes with age-related osteoporosis. Med Eng Phys 22(8):575–585
Krée P, Soize C (1986) Mathematics of random phenomena. Reidel, Dordrecht
Langer M, Pacureanu A, Suhonen H, Grimal Q, Cloetens P, Peyrin F (2012) X-ray phase nanotomography resolves the 3D human bone ultrastructure. PLoS One 7(8):e35691
Lewiecki EM (2013) Imaging technologies for assessment of skeletal health in men. Curr Osteoporos Rep 11(1):1–10
Link TM (2012) Osteoporosis imaging: state of the art and advanced imaging. Radiology 263(1):3–17
Manske SL, Liu-Ambrose T, Cooper DML, Kontulainen S, Guy P, Forster BB, McKay HA (2009) Cortical and trabecular bone in the femoral neck both contribute to proximal femur failure load prediction. Osteoporos Int 20(3):445–453
Mathieu V, Chappard C, Vayron R, Michel A, Haïat G (2013) Radial anatomic variation of ultrasonic velocity in human cortical bone. Ultrasound Med Biol 39(11):2185–2193
Matlab. Matlab R2007b documentation
Mayhew PM, Thomas CD, Clement JG, Loveridge N, Beck TJ, Bonfield W, Burgoyne CJ, Reeve J (2005) Relation between age, femoral neck cortical stability, and hip fracture risk. Lancet 366:129–135
Naili S, Vu MB, Grimal Q, Talmant M, Desceliers C, Soize C, Haiat G (2010) Influence of viscoelastic and viscous absorption on ultrasonic wave propagation in cortical bone: Application to axial transmission. J Acoust Soc Am 127(4):2622–2634
Nemat-Nasser S, Hori M (1999) Micromechanics: overall properties of heterogeneous materials, 2nd edn. Applied Mathematics and Mechanics. North-Holland
Nishiyama KK, Boyd SK (2011) In vivo assessment of trabecular and cortical bone microstructure. Clin Calcium 21(7):1011–1019
Nuzzo S, Peyrin F, Cloetens P, Baruchel J, Boivin G (2002) Quantification of the degree of mineralization of bone in three dimensions using synchrotron radiation microtomography. Med Phys 29(11):2672–2681
Parnell WJ, Vu MB, Grimal Q, Naili S (2012) Analytical methods to determine the effective mesoscopic and macroscopic elastic properties of cortical bone. Biomech Model Mechanobiol 11(6):883–901
Perilli E, Parkinson IH, Reynolds KJ (2012) Micro-CT examination of human bone: from biopsies towards the entire organ. Ann Ist Super Sanita 48(1):75–82
Predoi-Racila M, Crolet JM (2008) Human cortical bone: the sinupros model. Comput Methods Biomech Biomed Eng 11(2):169–187
Reisinger AG, Pahr DH, Zysset PK (2011) Elastic anisotropy of bone lamellae as a function of fibril orientation pattern. Biomech Model Mechanobiol 10(1):67–77

Rho J-Y, Kuhn-Spearing L, Zioupos P (1998) Mechanical properties and the hierarchical structure of bone. Med Eng Phys 20:92–102

Rossini M, Viapiana O, Adami S (1998) Instrumental diagnosis of osteoporosis. Aging 10(3):240–248

Rubinstein RY (1981) Simulation and the Monte Carlo method. Wiley, Hoboken

Sansalone V, Naili S, Bousson V, Bergot C, Peyrin F, Laredo JD, Haiat G (2010) Determination of the heterogeneous anisotropic elastic properties of human femoral bone: from nanoscopic to organ scale. J Biomech 43(10):1857–1863

Sansalone V, Bousson V, Naili S, Bergot C, Peyrin F, Laredo JD, Haiat G (2012a) Anatomical distribution of the degree of mineralization of bone tissue in human femoral neck: Impact on biomechanical properties. Bone 50(4):876–884

Sansalone V, Bousson V, Naili S, Bergot C, Peyrin F, Laredo JD, Haiat G (2012b) Effects of the axial variations of porosity and mineralization on the elastic properties of the human femoral neck. Comput Model Eng Sci 87(5):387–409

Sansalone V, Naili S, Desceliers C (2014) A stochastic homogenization approach to estimate bone elastic properties. CR Mec 342(5):326–333

Sasso M, Haiat G, Yamato Y, Naili S, Matsukawa M (2007) Frequency dependence of ultrasonic attenuation in bovine cortical bone: an in vitro study. Ultrasound Med Biol 33(12):1933–1942

Sasso M, Haiat G, Yamato Y, Naili S, Matsukawa M (2008) Dependence of ultrasonic attenuation on bone mass and microstructure in bovine cortical bone. J Biomech 41(2):347–355

Schrof S, Varga P, Galvis L, Raum K, Masic A (2014) 3D raman mapping of the collagen fibril orientation in human osteonal lamellae. J Struct Biol 187(3):266–275

Shannon C (1948) A mathematical theory of communication. Tech J 27, Bell Syst

Soize C (2001) Maximum entropy approach for modeling random uncertainties in transient elastodynamics. J Acoust Soc Am 109(5):1979–1996

Soize C (2006) Non-gaussian positive-definite matrix-valued random fields for elliptic stochastic partial differential operators. Comput Methods Appl Mech Eng 195(1–3):26–64

Soize C (2008) Tensor-valued random fields for meso-scale stochastic model of anisotropic elastic microstructure and probabilistic analysis of representative volume element size. Probab Eng Mech 23(2–3):307–323

Spiesz EM, Kaminsky W, Zysset PK (2011) A quantitative collagen fibers orientation assessment using birefringence measurements: Calibration and application to human osteons. J Struct Biol 176(3):302–306

Sreenivasan D, Watson M, Callon K, Dray M, Das R, Grey A, Cornish J, Fernandez J (2013) Integrating micro CT indices, CT imaging and computational modelling to assess the mechanical performance of fluoride treated bone. Med Eng Phys 35(12):1793–1800

Suquet P (ed) (1997) Continuum micromechanics. Number 377 in CISM lecture notes. Springer, Wien

Suvorov AP, Dvorak GJ (2002) Rate form of the Eshelby and Hill tensors. Int J Solids Struct 39(21):5659–5678

Tai K, Pelled G, Sheyn D, Bershteyn A, Han L, Kallai I, Zilberman Y, Ortiz C, Gazit D (2008) Nanobiomechanics of repair bone regenerated by genetically modified mesenchymal stem cells. Tissue Eng A 14(10):1709–1720

Vajda EG, Bloebaum RD (1999) Age-related hypermineralization in the female proximal human femur. Anat Rec 255(2):202–211

Valente G, Pitto L, Testi D, Seth A, Delp SL, Stagni R, Viceconti M, Taddei F (2014) Are subject-specific musculoskeletal models robust to the uncertainties in parameter identification? PLOS One 9(11):e112625

Varga P, Pacureanu A, Langer M, Suhonen H, Hesse B, Grimal Q, Cloetens P, Raum K, Peyrin F (2013) Investigation of the three-dimensional orientation of mineralized collagen fibrils in human lamellar bone using synchrotron X-ray phase nano-tomography. Acta Biomater 9(9):8118–8127

Vayron R, Barthel E, Mathieu V, Soffer E, Anagnostou F, Haïat G (2012) Nanoindentation measurements of biomechanical properties in mature and newly formed bone tissue surrounding an implant. J Biomech Eng 134(2):021007

Vayron R, Matsukawa M, Tsubota R, Mathieu V, Barthel E, Haïat G (2014) Evolution of bone biomechanical properties at the micrometer scale around titanium implant as a function of healing time. Phys Med Biol 59(6):1389–1406

Wagner DW, Lindsey DP, Beaupre GS (2011) Deriving tissue density and elastic modulus from microCT bone scans. Bone 49(5):931–938

Yamato Y, Matsukawa M, Otani T, Yamazaki K, Nagano A (2006) Distribution of longitudinal wave properties in bovine cortical bone in vitro. Ultrasonics 44(Suppl 1):e233–e237

Yao H, Dao M, Carnelli D, Tai K, Ortiz C (2011) Size-dependent heterogeneity benefits the mechanical performance of bone. J Mech Phys Solids 59:64–74

Yoon YJ, Cowin SC (2008a) The estimated elastic constants for a single bone osteonal lamella. Biomech Model Mechanobiol 7(1):1–11

Yoon YJ, Cowin SC (2008b) An estimate of anisotropic poroelastic constants of an osteon. Biomech Model Mechanobiol 7(1):13–26

Zebaze RM, Ghasem-Zadeh A, Bohte A, Iuliano-Burns S, Mirams M, Price RI, Mackie EJ, Seeman E (2010) Intracortical remodelling and porosity in the distal radius and post-mortem femurs of women: a cross-sectional study. Lancet 375(9727):1729–1736